ΠΑΝΕΠΙΣΤΗΜΙΟ ΚΡΗΤΗΣ
ΤΜΗΜΑ ΦΥΣΙΚΗΣ
ΜΕΤΑΠΤΥΧΙΑΚΟ ΠΡΟΓΡΑΜΜΑ
ΦΩΤΟΝΙΚΗΣ-ΝΑΝΟΗΛΕΚΤΡΟΝΙΚΗΣ


# ΜΟΡΙΑΚΗ ΔΥΝΑΜΙΚΗ ΜΙΚΡΩΝ ΣΥΣΤΗΜΑΤΩΝ ΧΡΗΣΙΜΟΠΟΙΩΝΤΑΣ ΦΩΣ ΚΑΙ ΗΛΕΚΤΡΟΝΙΑ

Αφεντάκη Αγγελική

Υπεύθυνος Ερευνητής: Σαμαρτζής Πέτρος

**ΗΡΑΚΛΕΙΟ 2019**

UNIVERSITY OF CRETE
PHYSICS DEPARTMENT
MASTER PROGRAM PHOTONICS-
NANOELECTRONICS


# MOLECULAR DYNAMICS OF SMALL SYSTEMS PROBED WITH LIGHT AND ELECTRONS

Afentaki Angeliki

Supervisor: Dr. Samartzis Petros

**HERAKLION 2019**

# ΠΕΡΙΛΗΨΗ

Η παρούσα μεταπτυχιακή εργασία περιλαμβάνει πειράματα κατά τα οποία μελετήθηκε ο κυκλικός διχρωισμός των φωτοηλεκτρονίων όταν ένα χειρόμορφο μόριο ιονίζεται από κυκλικά πολωμένο φως λέιζερ. Το μόριο το οποίο μελετήθηκε είναι το fenchone για ακτινοβολία σε διαφορετικά μήκη κύματος ώστε να διερευνηθεί η εξάρτηση του φαινομένου από το μήκος κύματος. Το κίνητρο για την παραπάνω έρευνα ήταν η επέκταση της γνώσης των χειρόμορφων μορίων και του τρόπου που αυτά αλληλεπιδρούν με το κυκλικά πολωμένο φως που στη συνέχεια θα χρησιμοποιηθεί στον προσδιορισμό και διαχωρισμό εναντιομερών. Η εργασία χωρίζεται σε 5 κεφάλαια.

Στο πρώτο κεφάλαιο, γίνεται μία σύντομη περιγραφή της θεωρίας που είναι απαραίτητη για την κατανόηση και την ερμηνεία των πειραμάτων που περιγράφονται στα επόμενα κεφάλαια. Συγκεκριμένα ο αναγνώστης εισάγεται στον τομέα της χημικής δυναμικής και γίνεται μια ανασκόπηση της βιβλιογραφίας για τον κυκλικό διχρωισμό φωτοηλεκτρονίων και τους τρόπους με τους οποίους ανιχνεύεται και αναλύεται.

Το δεύτερο κεφάλαιο, περιλαμβάνει μία λεπτομερή περιγραφή της πειραματικής διάταξης που χρησιμοποιήθηκε, τα επιμέρους στοιχεία της, τη μέθοδο απεικόνισης ιόντων καθώς και μία σύντομη επεξήγηση των δύο βασικών πληροφοριών που λαμβάνουμε από αυτήν, την κατανομή των ταχυτήτων και την γωνιακή κατανομή των μετρούμενων σωματιδίων.

Στο τρίτο κεφάλαιο, περιγράφουμε την ανάπτυξη μίας θερμαινόμενής παλμικής βαλβίδας που ήταν απαραίτητη στην πειραματική διάταξη, πώς λύθηκε αντίστοιχα από άλλα γκρουπ και τη μέθοδο που επιλέξαμε εμείς να την προσεγγίσουμε. Παρουσιάζονται όλα τα βήματα που ακολουθήθηκαν καθώς και το τελικό αποτέλεσμα.

Στο τέταρτο κεφάλαιο, περιγράφεται η διαδικασία επεξεργασίας και ανάλυσης των δεδομένων. Γίνονται κατανοητά τα επιμέρους προγράμματα που εκτελούνται, ο τρόπος με τον οποίο επεξεργάζονται τα δεδομένα και πώς ο ερευνητής αξιοποιεί τα αποτελέσματα που δίνουν.

Τέλος, στο πέμπτο κεφάλαιο, γίνεται μια αναφορά σε προηγούμενες μελέτες για το χειρόμορφο μόριο fenchone και στη συνέχεια παρατίθενται τα αποτελέσματά μας και πιθανές ερμηνείες. Τα πειράματα πραγματοποιήθηκαν για ένα εύρος μηκών κύματος διέγερσης όπου για κάθε μήκος κύματος λαμβάνονταν πληροφορίες και για τα τρία είδη πόλωσης του φωτός, γραμμική, δεξιόστροφη και αριστερόστροφη κυκλική πόλωση. Στα αποτελέσματα εμπεριέχονται τυχόν διαφοροποιήσεις των δύο εναντιομερών του μορίου, συγκρίνονται με τα θεωρητικά αναμενόμενα αποτελέσματα και ερχόμαστε ένα βήμα πιο κοντά στην επίτευξη μίας γενικής μεθόδου προσδιορισμού των δύο εναντιομερών ενός χειρόμορφου μορίου.

# ABSTRACT

This Master Thesis contains experiments in which photoelectron circular dichroism (PECD) is studied when a chiral molecule gets ionized by circularly polarized laser radiation. The under-study chiral molecule is fenchone, and the radiation was used in different wavelengths in order to examine the wavelength dependence of this phenomenon. The motivation for this investigation was the extension of the knowledge around chiral molecules and the way they interact with circularly polarized light. This will be next used to detect and separate enantiomers. The thesis is divided in 5 Chapters.

Chapter 1 provides a brief introduction of the theory which is necessary for the understanding and the interpretation of the experiments described on the following chapters. Specifically, the reader is introduced to the field of chemical dynamics and a review of the results of former experiments on PECD and several ways that this is probed and analyzed are presented.

The second chapter consists of a detailed presentation of the experimental setup used in this work, its individual parts, the ion imaging technique as well as a brief explanation of the main information gained: the speed and angular distribution of the measured particles.

In the third part of this thesis, we demonstrate the development of a heated nozzle, the way other groups performed the heating and the method we chose to approach it. All the necessary steps are included as well as the final result.

In chapter four, the procedure of editing and analyzing the data with several different programs is described. Each step is explained thoroughly, the way the programs process the data and how a researcher uses them are in addition included.

In the last chapter, there's a review on previous work on PECD for the chiral molecule fenchone and afterwards, our results and possible interpretationof them are presented. The experiments were conducted for a wide range of wavelengths and for each one we recorded information for the three polarization states, linear, right and left circular polarization. The two enantiomers of the molecule are studied separately and their results are discussed and compared with theoretical calculations. This contribution paves the way to accomplish a generalized enantiospecific method for every chiral molecule.

# Contents

# Chapter 1-Introduction

## 1.1 Chirality

Chirality is the ability of chemical molecules to exist as a pair of non-superimposable mirror images.
One molecule of the pair is known as the left and the other as the right enantiomer. Both enantiomers have the same chemical and physical properties (melting point, boiling point etc.) but also properties that are different: they cannot have a plane of symmetry so they cannot be divided in two mirror-image halves and they have optical activity.[1]

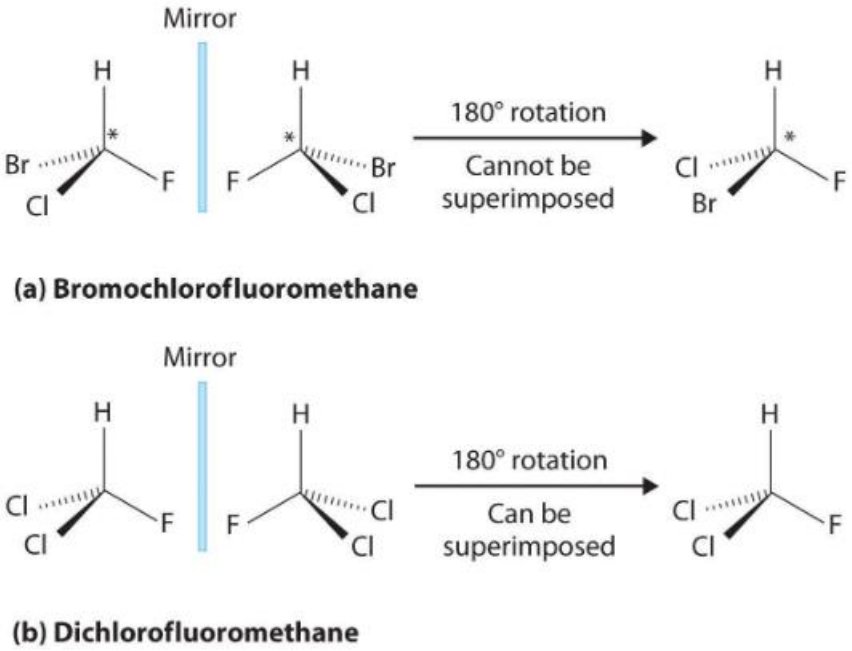


***Figure 1.1:Comparison of Chiral and Achiral Molecules. (a) Bromochlorofluoromethane is a chiral molecule whose stereocenter is designated with an asterisk. Rotation of its mirror image does not generate the original structure. To superimpose the mirror images, bonds must be broken and reformed. (b) In contrast, dichlorofluoromethane and its mirror image can be rotated so they are superimposable. [2]***

Optical activity is the rotation of the orientation of the plane of polarization about the optical axis of linearly polarized light as it travels through materials. It occurs only in chiral materials, those lacking microscopic mirror symmetry. This optical activity is what we're taking advantage of in this work. It depends on several factors such as the concentration of the sample, temperature and wavelength of the light used. Rotation is given in +/- degrees depending on whether the sample has d- (positive) or l- (negative) enantiomers. The standard measurement for rotation for a specific chemical compound is called the specific rotation, defined as an angle measured at a path length of 1 decimeter and a concentration of 1g/ml. The specific rotation of a pure substance is an intrinsic property. In solution, the formula for specific rotation is:

$$[a]_{\lambda}^{T} = \frac{a}{l \cdot c} \tag{1.1}$$

where

- [a] is the specific rotation in degrees $cm^3\ dm^{-1}g^{-1}$.
- λ is the wavelength in nanometers,
- α is the measured angle of rotation of a substance,
- T is the temperature in degrees,
- l is the path length in decimeters and
- c is the concentration in g/ml.

Molecular chirality is often studied by chirooptical techniques such as circular dichroism in absorption in which tiny differences ($10^{-3}$ – $10^{-5}$) in the relative absorption between left- and right-handed Circularly-Polarized Light, for a given enantiomer, is observed [3,4,5]. Another technique to study chirality is chiral chromatography where two diastereomeric adducts with different physiochemical properties are formed during elution. The adducts differ in their stability and/or in their interphase distribution ratio [6]. Additional methods that have been proposed are based upon Coulomb Explosion Imaging, [7,8] a polarized microwave double resonance technique in which the detected phase discriminates enantiomers, [9,10] or Nuclear Magnetic Resonance (NMR) Crystallography, [11] that uses the concepts of supramolecular chemistry where non-covalent interactions between molecules such as hydrogen bonding, electrostatic or van der Waals forces play important roles in the properties and shape of a molecular assembly.

## 1.2 Photoelectron Circular Dichroism (PECD)

Photoelectron Circular Dichroism (PECD) arises from a front-back asymmetry (along the light propagation direction) in the angular distribution of photoelectrons emitted from randomly oriented molecular enantiomers in gas phase, when these are ionized by circularly polarized radiation [2]. In Figure 2 a typical image of that asymmetry is shown.

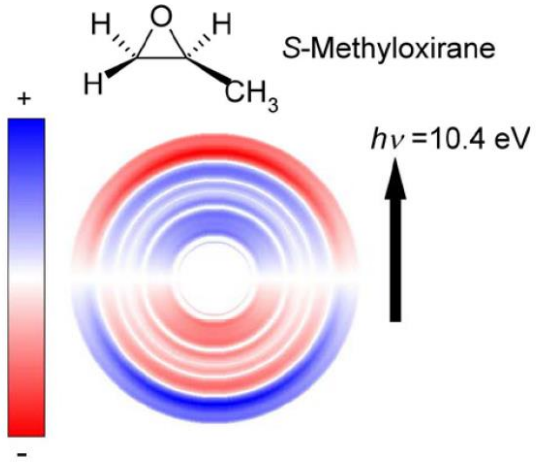


***Figure 1.2: Detecting chirality in molecules by imaging photoelectron circular dichroism.***[12]

In a single photon excitation process the angular distribution of the fragments ejected from the randomly oriented chiral molecule is given by [2]:

$$I_{lin}(\theta) = 1 + \beta P_2(cos\theta) \quad (1.2)$$
$$I_{cpl}(\theta) = 1 - (\beta/2)P_2(cos\theta) \quad (1.3)$$

Equation 1.2 refers to linearly polarized light, where θ is the ejection angle measured with respect to the electric field vector and Eq. (1.3) applies to circular polarization, where θ is the angle measured relative to the photon propagation direction. The function $P_2$ is the second Legendre polynomial. The general equation of the Legendre polynomials is $P_n(x) = \frac{1}{2^n n!}\frac{d^n}{dx^n}(x^2-1)^n$ and first orders are [13]:

| n | $P_n(x)$ |
|---|---|
| 0 | $1$ |
| 1 | $x$ |
| 2 | $\frac{1}{2}(3x^2-1)$ |
| 3 | $\frac{1}{2}(5x^3-3x)$ |
| 4 | $\frac{1}{8}(35x^4-30x^2+3)$ |
| 5 | $\frac{1}{8}(63x^5-70x^3+15x)$ |
| 6 | $\frac{1}{16}(231x^6-315x^4+105x^2-5)$ |
| 7 | $\frac{1}{16}(429x^7-693x^5+315x^3-35x)$ |
| 8 | $\frac{1}{128}(6435x^8-12012x^6+6930x^4-1260x^2+35)$ |
| 9 | $\frac{1}{128}(12155x^9-25740x^7+18018x^5-4620x^3+315x$ |
| 10 | $\frac{1}{256}(46189x^{10}-109395x^8+90090x^6-30030x^4+3465x^2-63)$ |

The parameter β takes a value ranging from -1 to +2 [2]. These limits for linear polarization correspond, respectively, to pure $\sin^2$ or $\cos^2$ distributions while β=0 corresponds to anisotropic distribution (Fig. 1.3).

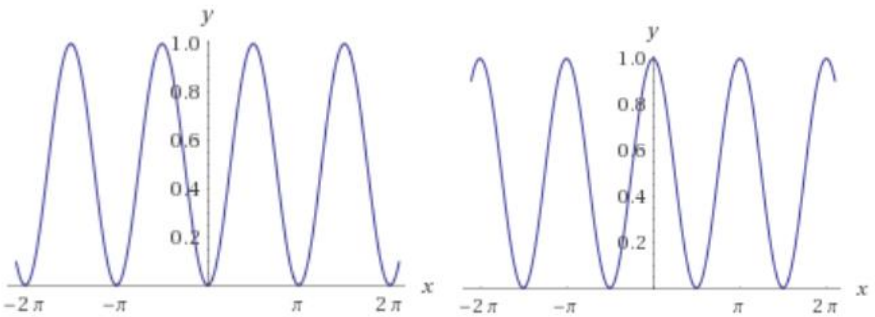


***Figure 1.3: The $\sin^2$(left) and $\cos^2$(right) distributions.***

Therefore, β characterizes the anisotropy of the distribution and is commonly referred to as anisotropy parameter [2]. Those two equations are sub-cases of a more general form. It was first

proposed by Ritchie [14] that even in the pure electric-dipole approximation the general photoionization electron angular distribution function normalized over the surface of a unit sphere for n-photon ionization is:

$$I_p(\theta) = 1 + \sum_{i=1}^{2n} b_i^{\{p\}} P_i(cos\theta) \tag{1.4}$$

where $P_i$ is the i-th Legendre polynomial. The coefficients $b_i^{\{p\}}$ depend on the polarization which is expressed by the superscript p (p=0 for linear polarization, p=$\pm$1 for left, right circular polarization) and the following symmetry relationships apply [***14,15***]:

$$b_1^{\{0\}} = 0 \tag{1.5}$$
$$b_1^{\{+1\}} = -b_1^{\{-1\}} \tag{1.6}$$
$$b_2^{\{0\}} = -(1/2) b_2^{\{\pm 1\}} \tag{1.7}$$

Combining Eq. (1.5) and Eq. (1.4) results in the familiar form of Eq. (1.2) for n=1. For linear polarization $b_2^{\{0\}}$ is equivalent to the β anisotropy parameter. Eq. (1.7) also explains the additional prefactor of -1/2 that occurs for circular polarization, as seen in Eq. (1.3).

Eq. $b_1^{\{p\}} = 0$ is general and applies to any polarization for achiral molecules [2]. The nonzero values of these variables appear only for circular polarization and chiral molecules. This non-equivalence results from the ±1 spherical tensor components of the photoionization matrix elements when the molecular potential has a specific orientation. Hence, a forward–backward asymmetry in the angular distribution can be anticipated as θ swings through 90°. Furthermore, the antisymmetry of $b_1^{\{\pm 1\}}$(Eq. 1.6) leads to a reversal of the forward–backward asymmetry when the helicity of the radiation is exchanged (from right circularly polarization to left and vice versa). This contributes to the circular dichroism (or difference between responses to left- (LCP) and right-handed (RCP) circular polarization in the angle-resolved photoelectron distribution). The same reversal is anticipated when the handedness of the enantiomeric molecule is exchanged.

It is more common to examine the dichroism, i.e. the difference between the opposite helicities (right or left) of polarized light or of the enantiomer, so that the signal is stronger and easier to process. In addition, the sensitivity is improved as noise present in both RCP and LCP images is cancelled out. From Eq. (1.4) and Eq. (1.6) the expression for the difference is [2,19]:

$$I_{lcp}(\theta) - I_{rcp}(\theta) = \sum_{i=1}^{n} 2 b_{2i-1}^{\{+1\}} P_{2i-1}(cos\theta) \tag{1.8}$$

The symmetry properties of the Legendre coefficients in multiphoton ionization have been observed experimentally [16,17,18]. For multiphoton ionization the difference angular distributions (the right part of Eq. 1.8) contain contributions of Legendre polynomials up to order (2n-1). For instance, for a three-photon ionization the coefficients $b_1^{\{+1\}}$, $b_3^{\{+1\}}$and $b_5^{\{+1\}}$ determine the shape of Eq. (1.8). Depending on the relative size of the odd coefficients, the maxima and the minima of function (1.8) will be found at various angles θ that may differ from the single-photon case, where the extrema are always at θ=0 and θ=π.

It's important to note that multiphoton ionization has the added advantage that by selecting the wavelength of the excitation one can ionize through resonant excited states. Excitation through an

intermediate state my spatially align the molecule before ionization, which could potentially enhance the enantiomeric selectivity of the PAD measurement.

## 1.3 Experimental Approach: Imaging PECD

The key observable for photoelectron circular dichroism is the energy and differential cross section of photoelectrons ejected after photoionization. The desired dynamical information would be obtained in the parameters $b_i^{\{\pm 1\}}$, i=1, 3, …, which can then, as argued above, be used to quantify the observed PECD asymmetry. In principle, values for these $b_i^{\{\pm 1\}}$parameters could be obtained by fitting a single measured angular distribution. In practice, this is not usually attempted and instead the dichroism or difference observed between two measurements made with LCP and RCP is examined (or between R- and S- enantiomers), exploiting the symmetry properties of the $b_i^{\{\pm 1\}}$ coefficients.

The first one-photon PECD experiments in the Vacuum Ultra Violet (VUV) and Soft X-Ray (SXR) spectral regions used one or more dispersive electron analyzers at fixed observation angle to the light beam [20,21] and fitted the dichroism with Eq. (8). The number of experiments measuring the angular resolved momentum distribution of charged particles (electrons or ions) has expanded enormously during the last 32 years since the first demonstration of ion imaging in 1987 by Chandler and Houston [22]. The detailed molecular dynamics information obtained by measuring the kinetic energy and angular distribution of electrons and ions, has stimulated the continuous improvement of these powerful imaging techniques. One such improvement is the electron-ion coincidence imaging detection [23] that is particularly useful for enantiomer separation using PECD.

In the original first report of ion imaging in 1987 [24] the initial three-dimensional velocity distribution of a recoiling ion was projected (imaged) onto a two-dimensional single particle detector: a Micro-Channel-Plate (MCP) followed by a phosphor screen and a digital Charge-Couple-Device (CCD) camera. The three-dimensional distribution is reconstructed by use of mathematical algorithms, like the inverse Abel transformation in case of cylindrical symmetry and other image inversion techniques (singular value decomposition [25]).

In 1997, Eppink and Parker [26] introduced open (grid-less) electrodes that act like electrostatic lenses, to map the velocity of the particles from an extended source region onto a spot of the detector. This is now referred to as Velocity Map Imaging (VMI). If the ion extraction field and the detector are gated, using switched extraction fields, then it's feasible to measure directly the three-dimensional distribution. This was first introduced by Kitsopoulos and co-workers [27] and is called slice-imaging. Photoelectrons usually have only a very small arrival-time spread between the forward and backward part of the Newton sphere [28], typically only about 1-5 nanoseconds. This makes it extremely challenging to measure a slice through the 3D-distribution with ns lasers. That led to the use of very short duration light sources like femtosecond or picosecond lasers in combination with fast timing electronics to be feasible to measure directly the arrival time of photoelectrons along the time-of-flight direction.

PECD is a chirooptical effect which was theoretically predicted in the 1970s [14]. Most chirooptical phenomena are based on magnetic or electric quadrupole effects whereas PECD can be interpreted completely by the electric dipole approximation. As a result, PECD is several orders of magnitude larger than conventional chiroptical effects, which are in general extremely weak and difficult to use for studies in gas-phase samples. The first experimental observation of PECD from an ensemble of randomly oriented chiral molecules was performed in 2001 using Vacuum Ultra Violet (VUV) synchrotron radiation.[29] Since then, many studies relying on single photon ionization have been conducted, showing that PECD is a powerful probe of molecular chirality. Single photon PECD experiments could be performed using femtosecond elliptically polarized VUV sources and also the use of UV, visible and IR femtosecond laser sources is feasible [30].

Several chiral molecules have been studied over the years with the interest mostly turned in camphor, fenchone, limonene, methyl- and trifluoromethyl-oxirane and glycidol.
In 2006 Bowering *et al.* used synchrotron radiation on camphor which helped to determine that in the HOMO−1 channel (highest occupied molecular orbital) the PECD chiral asymmetry curves show a double maximum reaching nearly 10% close to threshold energy and peaking again at 20% some 11 eV above threshold. This was attributed to a resonance that is also visible in the $b_1^{\{+1\}}$ parameter[31]. Two years later, Powis *et al.*[32] performed PECD experiments in the valence ionization of selected enantiomers both on camphor and fenchone using synchrotron radiation, too. Theoretical modeling of the results using electron scattering calculations demonstrated that the observed chiral asymmetry in the photoelectron angular distributions depends strongly upon the final state scattering, and upon the quality of the molecular potential used for these calculations. Nevertheless, very pronounced dependence on the orbital from which ionization occurs was also observed. Comparison with analogous results for camphor [33] reveals striking differences in the PECD. PECD measurements readily differentiate these molecules despite their very similar photoelectron spectra, demonstrating PECD to be a structurally sensitive probe. A couple of years later, Nahon, Garcia *et al*. [34] focused on mass selection on camphor which corresponds to size selection of the nascent species monomer and dimer. Taking advantage of this, they initiated studies of the valence-shell angular distribution of photoelectrons from size selected molecular dimers. The results show that the anisotropy parameter β, is insensitive to dimerization. PECD measurements were conducted in 2014 [35], using femtosecond laser pulses at 795nm on camphor, fenchone and norcamphor and proved that even though those molecules look alike they respond differently to PECD. This may hint to the importance of the scattering state for this relatively low kinetic energy electrons released in the multiphoton process. In 2016 additional experiments were performed on these isomers with VUV synchrotron radiation[36] that can be used as benchmarking data for new experiments as well as theoretical models due to the chromatographic technique used. At the same time Lux *et al.*[37] used fs laser pulses, ionized with three photons to threshold and compared with four photon ionization above threshold as Muller *et al.* [38] did at different wavelengths. Most recently Beaulieu [39] introduced photoexcitation circular dichroism (uses the coherent helical motion of bound electrons excited by ultra-short circular polarized light) at 201nm with fs laser pulses and concluded that the existence of the enantio-sensitive macroscopic dipole opens a way to laser driven separation of enantiomers in isotropic racemic mixtures in the gas phase.

Turchini *et al*. performed temperature dependent PECD on 3 methyl cyclopentanone using synchrotron radiation and they managed to separate the contribution of each conformer to the dichroism revealing the individual dispersions as a function of the photoelectron kinetic energy [40].
Powis concerned himself with carvone using synchrotron radiation and showed that PECD depends on molecular conformation and on which orbital it is being ionized [41]. The group of Pitzer, Schmidt *et al*., focused on carbon monoxide [42] and proved that circular dichroism of the ionizing photon is fully transferred to the remaining ion, whose degenerate electronic states with well-defined magnetic quantum number become oriented (polarized). On the contrary, non-degenerate electronic states of chiral molecules without any symmetry (C1-symmetry) cannot be oriented by circularly polarized radiation. Further investigation has been conducted in butanediol [43], monoterpene [44], isopropanolamine [45], epichlorohydrin [46]and to a metal-organic complex Δ-Cobalt (III) tris-acetylacetonate [47] with synchrotron radiation and all of the results are in agreement with the theoretical calculations.
Extensive work has been done on methyloxirane (MOX) and trifluoromethyloxirane (TFMOX). Ilchen's *et al*. [48] calculations demonstrate strong dispersions of the dichroic parameters $\beta_1$ for O and individual F atoms in triuoromethyloxirane, which for some photoelectron energies reach about 9%. For the oxygen K-edge, this theoretical result is in full agreement with the experiment. In order to compare theoretical and experimental results for the fluorine K-edge, the computed data were additionally averaged over the three F atoms. This results in a considerable drop of the maximal value of $\beta_1$down to about 2%. The experiment was performed with soft X-rays and velocity map

imaging spectroscopy. Garcia, Dossmann *et al*. [49], [50] abutted that the PECD signal is strongly influenced by the excitation of vibrational mode in the cation formation. The two molecules examined, methyloxirane and its trifluoromethyl analogue, are clearly related, yet maintain dissimilarities in their overall photoionization detail and in the detail of the vibrationally induced PECD structure. Using electron-ion coincidence techniques they measured the electron spectroscopy and the different fragmentation pathways have been identified as a function of the internal energy of the parent. In both molecules, the HOMO does not fragment and displays clear vibrational structure. In 2014 Fanood *et al*. [51] performed multi-photon PECD on these enantiomers using a Titanium: Sapphire femtosecond laser system at 420nm and electron-ion coincidence detection methods. The results complement previous work that has been done and also help characterize the different ionization channels. Three years later Tia, Pitzer *et al*. [52] performed studies on now uniaxially oriented methyloxirane enantiomers instead of randomly oriented and indicated that distinct spatial configurations of a chiral molecule enhance the PECD signal by a factor of 10.

In 2014 Powis *et al*. [53] used synchrotron radiation on homochiral clusters of glycidol enantiomers. The PECD signal effectively carries the signature of the neutral precursor species, prior to any fragmentation of the ion, as may be inferred from the below monomer threshold measurements where the monomer's direct ionization channel is closed, and so it must share a common parentage, proceeding from the dimer (or higher) clusters. Another work in pure glycidol enantiomers[54], showed that the influence of intramolecular hydrogen bond orbital polarization is found to play a small yet significant role in determining the chiral asymmetry in the electron angular distributions. Tia *et al*. [55]used two different vaporization methods on Alanine and then dichroism studies helped as diagnostics to evaluate them. A much bigger molecule, limonene, has also attracted much interest although it was shown [56] with femtosecond laser that PECD is insensitive to the electronic character and the oscillator strength of resonances involved in multi photon ionization in the UV range. On the contrary, a rich vibrational structure was displayed in the threshold photoelectron spectrum with the PECD signal using synchrotron radiation [57] found to be strongly dependent on the vibronic structure appearing in the photoelectron spectra, with the observed asymmetry even switching direction in between the major vibrational peaks. This effect can be ultimately attributed to the sensitivity of this dichroism to small phase shifts between adjacent partial waves of the outgoing photoelectron. In 2018 [30] two-color laser fields were used in an attempt to decouple the role of bound-bound and bound-continuum transitions in REMPI (resonance enhanced multiphoton ionization) PECD on limonene. They showed that the angular distribution of PECD strongly depends on the anisotropy of photoexcitation to the intermediate state, which is different for circularly and linearly polarized laser pulses. On the contrary, the helicity of the pulse that drives the bound-bound transition is shown to have a negligible effect on the PECD.

References

[1] https://chem.libretexts.org.
[2] I. Powis, ChemInform, vol. 39, no. 29, **2008**.
[3] C. Logé, U. Boesl, Phys. Chem. Chem. Phys. 14, **2012**, 11981.
[4] P. Horsch, G. Urbasch, K. Weitzel, Chirality 24, **2012**, 684.
[5] A. Hong, C.M. Choi, H.J. Eun, C. Jeong, J. Heo, N.J. Kim, Angew. Chem. Int. Ed.53,**2014**, 7805.
[6] L.Lepri, M. Del Bubba Encyclopedia of Seperation Science,**2000**, 2426-2440.
[7] M. Pitzer, M. Kunitski, A.S. Johnson, T. Jahnke, H. Sann, F. Sturm, L.P.H.Schmidt, H. Schmidt-Böcking, R. Dörner, J. Stohner, J. Kiedrowski, M. Reggelin,S. Marquardt, A. Schießer, R. Berger, M.S. Schöffler, Science 341, **2013**, 1096.
[8] P. Herwig, K. Zawatzky, M. Grieser, O. Heber, B. Jordon-Thaden, C. Krantz, O.Novotn´y, R. Repnow, V. Schurig, D. Schwalm, Z. Vager, A. Wolf, O. Trapp, H.Kreckel, Science 342, **2013**, 1084.
[9] V.A. Shubert, D. Schmitz, D. Patterson, J.M. Doyle, M. Schnell, Angew. Chem.Int. Ed. 53, **2014**, 1152–1155.
[10] D. Patterson, M. Schnell, J.M. Doyle, Nature 497,**2013**, 475.
[11] J. Labuta *et al.*, *Nat. Commun.*, **2013**, 4, 2188.
[12] M. H. M. Janssen and I. Powis, Phys. Chem. Chem. Phys.,**2014**, vol. 16, no. 3, pp. 856–871.
[13] Abramowitz, Milton, Stegun, Irene Ann, eds. **1983**, "Chapter 8". Handbook of Mathematical Functions with Formulas, Graphs, and Mathematical Tables. Applied Mathematics Series. **55** Washington D.C.; New York: United States Department of Commerce, National Bureau of Standards; Dover Publications. pp. 332, 773.
[14] B Ritchie Phys. Rev. A 13, 1411,**1976**.
[15] I. Powis, J. Chem. Phys. 112 (1), 301 ,**2000**.
[16] C. S. Lehmann, N. B. Ram and M.H.M. Janssen, European Phys. Journal Web of Conferences, **2013**, 41, 02029.
[17] C. S. Lehman, N. B. Ram, I. Powis and M. H. Janssen, J. Chem. Phys.,J Chem Phys. **2013,** 21, 139(23):234307.
[18] C. Lux, M. Wollenhaupt, T. Bolze, Q. Q. Liang, J Kohler, C. Sarpe and T. Baumert, Angew. Chem. Int. Ed., **2012**, 51, 5001.
[19] M. H. Janssen and I. Powis, Phys. Chem.Chem. Phys., **2013**.
[20] T. Lischke, N. Böwering, B. Schmidtke, N. Müller, T. Khalil, and U. Heinzmann, Phys. Rev. A - At. Mol. Opt. Phys., vol. 70, no. 2, pp. 1–12, **2004**.
[21] P. Decleva, T. Prosperi, I. Metodologie, S. Montelibretti, and M. Stazione, Phys.Rev.A. vol. 014502, pp. 1–4, **2004**.
[22] D. W. Chandler and P. L. Houston, **1987**, vol. 87, 1445.
[23] Monroe E., Annangudi S., Hatcher N., Gutstein H., Rubakhin S., Sweedler J.,**2008**, Proteomics. 8 (18), 3746–3754.
[24] A. T. J. B. Eppink and D. H. Parker, Rev. Sci. Instr., **1997**, 68, 3477.
[25] Boardman, Joe W., **1989**, document id: 19910031238.
[26] A. T. J. B. Eppink and D. H. Parker, Rev. Sci. Instr., **1997**, 68, 3477.
[27] C. R. Gebhardt, T. P. Rakitzis, P. C. Samartzis, V. Ladopoulos, T. Kitsopoulos, and C. R. Gebhardt, vol. 3848, no. September 2001, **2003**.
[28] I. Newton, Philosophiae Naturalis Principia Mathematica. London., , **1687** pp. Theorem XXXI.
[29] N. Böwering, T. Lischke, B. Schmidtke, N. Müller, T. Khalil, and U. Heinzmann, Phys. Rev. Lett., vol. 86, no. 7, pp. 1187–1190, **2001**.
[30] S. Beaulieu *et al.*, *J. Chem. Phys.*, vol. 149, no. 13, **2018**.
[31] L. Nahon, G. A. Garcia, C. J. Harding, E. Mikajlo, and I. Powis, J. Chem. Phys., vol. 125, no. 11, **2006**.
[32] I. Powis, C. J. Harding, G. A. Garcia, and L. Nahon, ChemPhysChem, vol. 9, no. 3, pp. 475–

483, **2008**.
[33] T. Lischke, N. Bηwering, B. Schmidtke, N. Muller, T. Khalil, U. Heinzmann,Phys. Rev. A,**2004**, 70, 022507.
[34] L. Nahon, G. A. Garcia, H. Soldi-Lose, S. Daly, and I. Powis, Phys. Rev. A - At. Mol. Opt. Phys., vol. 82, no. 3, pp. 1–10, **2010**.
[35] C. Lux, M. Wollenhaupt, C. Sarpe, and T. Baumert, ChemPhysChem, vol. 16, no. 1, pp. 115–137, **2015**.
[36] L. Nahon *et al.*, Phys. Chem. Chem. Phys., vol. 18, no. 18, pp. 12696–12706, **2016**.
[37] C. Lux, A. Senftleben, C. Sarpe, M. Wollenhaupt, and T. Baumert, *J.* Phys. B At. Mol. Opt. Phys., vol. 49, no. 2, **2015**.
[38] A. D. Müller, A. N. Artemyev, and P. V. Demekhin, *J. Chem. Phys.*, vol. 148, no. 21, **2018**.
[39] S. Beaulieu *et al.*, Nat. Phys., vol. 14, no. 5, pp. 484–489, **2018**.
[40] S. Turchini *et al.*, *ChemPhysChem*, vol. 14, no. 8, pp. 1723–1732, **2013**.
[41] A. Couture, E. Deniau, and P. Grandclaudon, vol. 216, no. May 2009, pp. 212–216, **2010**.
[42] M. Pitzer *et al.*, *Molecules*, vol. 23, no. 7, pp. 1–9, **2018**.
[43] S. Daly, I. Powis, G. A. Garcia, M. Tia, and L. Nahon, *J. Chem. Phys.*, vol. 147, no. 1, **2017**.
[44] H. Ganjitabar, R. Hadidi, G. A. Garcia, L. Nahon, and I. Powis, *J. Mol. Spectrosc.*, vol. 353, pp. 11–19, **2018**.
[45] D. Catone *et al.*, *Chem. Phys.*, vol. 482, pp. 294–302, **2017**.
[46] S. Daly, I. Powis, G. A. Garcia, H. Soldi-Lose, and L. Nahon, *J. Chem. Phys.*, vol. 134, no. 6, **2011**.
[47] D. Catone *et al.*, *Rend. Lincei*, vol. 24, no. 3, pp. 269–275, **2013**.
[48] M. Ilchen *et al.*, *Phys. Rev. A*, vol. 95, no. 5, **2017**.
[49] G. A. Garcia, H. Dossmann, L. Nahon, S. Daly, and I. Powis, Phys. Chem. Chem. Phys., vol. 16, no. 30, pp. 16214–16224, **2014**.
[50] G. A. Garcia, H. Dossmann, L. Nahon, S. Daly, and I. Powis,*ChemPhysChem*, vol. 18, no. 5, pp. 500–512, **2017**.
[51] M. M. Rafiee Fanood, I. Powis, and M. H. M. Janssen, *J. Phys. Chem. A*, vol. 118, no. 49, pp. 11541–11546, **2014**.
[52] M. Tia *et al.*, *J. Phys. Chem. Lett.*, vol. 8, no. 13, pp. 2780–2786, **2017**.
[53] I. Powis, S. Daly, M. Tia, B. Cunha De Miranda, G. A. Garcia, and L. Nahon, *Phys. Chem. Chem. Phys.*, vol. 16, no. 2, pp. 467–476, **2014**.
[54] G. A. Garcia, L. Nahon, C. J. Harding, and I. Powis, *Phys. Chem. Chem. Phys.*, vol. 10, no. 12, pp. 1628–1639, **2008**.
[55] M. Tia *et al.*, *J. Phys. Chem. A*, vol. 118, no. 15, pp. 2765–2779, **2014**.
[56] S. Beaulieu,A. Ferré, R. Géneaux, R. Canonge,D. Descamps, B. Fabre,N. Fedorov,F. Légaré, S. Petit,T. Ruchon,V. Blanchet,Y. Mairesse and B. Pons, *New J. Phys.*, vol. 18, no. 10, **2016**.
[57] M. M. Rafiee Fanood, H. Ganjitabar, G. A. Garcia, L. Nahon, S. Turchini, and I. Powis, *ChemPhysChem*, vol. 19, no. 8, pp. 921–933, **2018**.

# Chapter 2 – Experimental Setup

In this work we're studying the PECD effect as it has already been mentioned. In order to do so, there is the need of a molecular beam, laser systems to ionize the molecules, vacuum systems, etc. that will be described in detail in this chapter. The imaging technique we're using is Velocity Map Imaging (VMI) first proposed by Eppink and Parker in 1997. The operating principle of VMI [1] is shown in Figure 2.1.

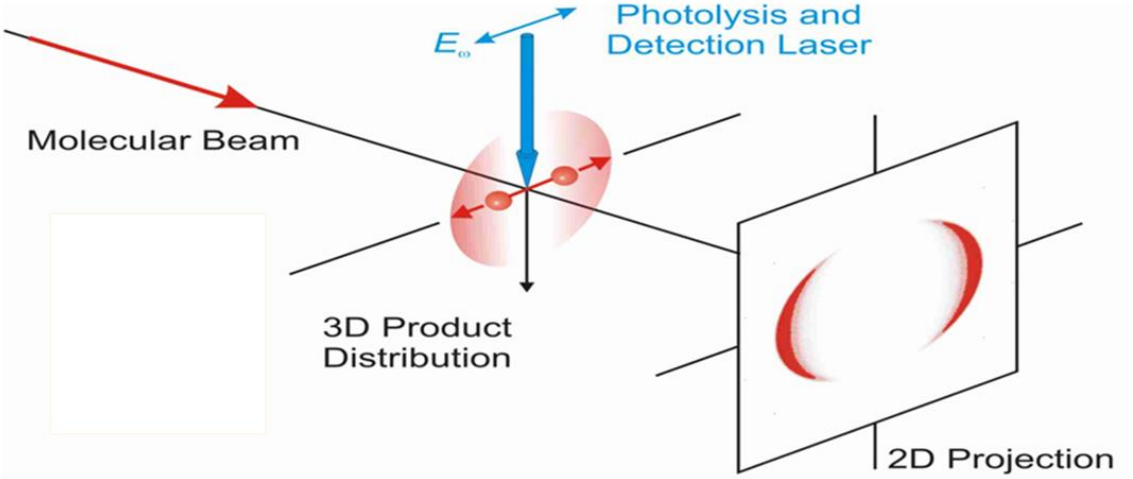


***Figure 2.1: Velocity Map Imaging setup.***

The molecular beam, which will be discussed more thoroughly in section 2.2, is intersected at right angles by a laser beam that photoionizes the target molecules. The Newton sphere of the photoelectrons produced gets accelerated by an electric field and then propagates a field-free time-of-flight (TOF) space and projects on a position-sensitive detector. Detector images are recorded by a CCD camera and processed with the use of inverse Abel transform to produce the two-dimensional cut through the center of the original 3D distribution. From the analysis of this image we can get information regarding the kinetic energy release and the angular distribution of the photoelectrons. A schematic of the exact setup that was used in the experiments is shown in Figure 2.2.

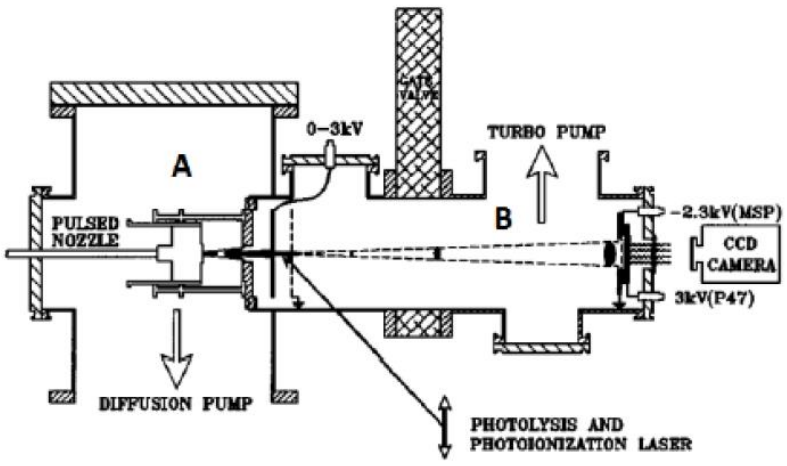


***Figure 2.2: Schematic representation of the experiment apparatus.***

## 2.1 Vacuum System

The apparatus consists of two differentially pumped chambers, source chamber (Region A) and detector chamber (Region B). The two regions are maintained in high vacuum ($10^{-6}$ – $10^{-7}$ Torr). The source chamber is pumped by a baffled 3000 L/s oil diffusion pump (Leybold, DI 3000) that is backed by a Leybold Trivac D65B rotary mechanical pump at a speed of $65 m^3/h$. The detector chamber is pumped by a 600 L/s turbo-molecular pump (Leybold, Turbovac 600) that is backed by a Leybold Trivac D25B rotary pump with pumping speed of $25 m^3/h$.[2]

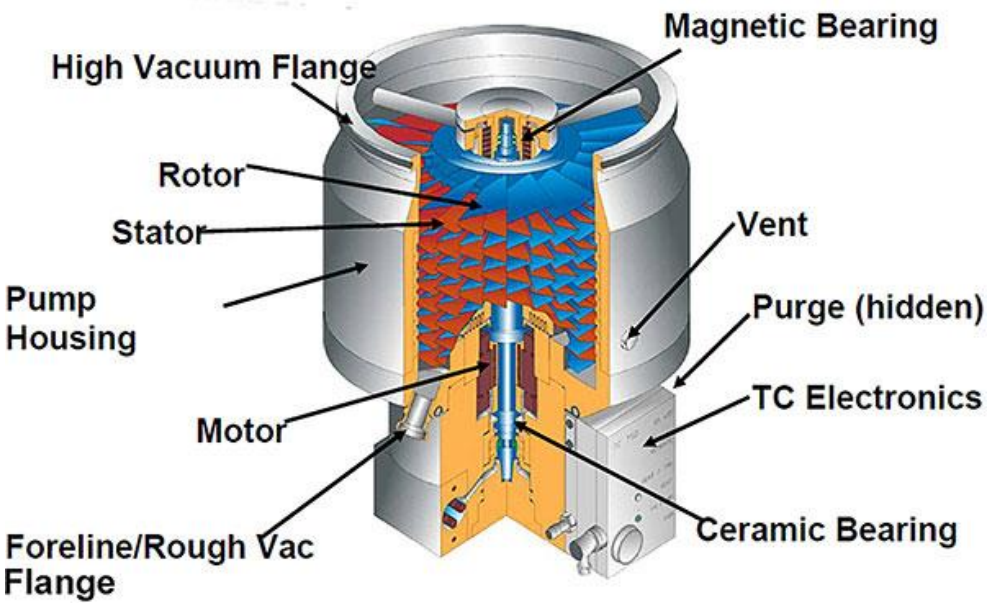


***Figure 2.3: Cutaway view of a turbomolecular pump. The blades in blue rotate and the red blades are static. [3]***

## 2.2 Molecular Beam

It is important for the reactant molecules to have very well-defined conditions regarding their velocity and internal energy. In order to assure that the molecules are in a known quantum state, we are cooling them in a collision-full environment forming a molecular beam. This is achieved in the following way: The molecules under-study are seeded in an inert carrier gas and the mix expands through the nozzle into the source vacuum chamber. A skimmer is placed after the nozzle orifice to collimate the beam. The expansion of the gas proceeds adiabatically, resulting in a cold molecular beam.

During the expansion through the nozzle, energy transfer occurs between the gas molecules through collisions. Exactly after the nozzle there is a zone called “silent zone” where the molecules travel with supersonic speeds -faster than the speed of sound-, in a parallel manner, and no collisions occur. These are the ideal conditions of the beam and they are maintained with the skimmer placed inside the silent zone. [4]

The supersonic beam ensures that the molecules are prepared in their ground electronic and lower few rotational states (rotational temperature 10-30K). Vibrational cooling happens in a lesser extent because the spacing between adjacent low-lying vibrational levels is usually larger that the collision energy of the expanding molecules. Under no cluster formation conditions, the final velocity of the molecular beam is determined by the mass of the carrier gas molecules. [5]

In our case, the molecular beam is generated by a home-built pulsed, piezoelectrically actuated,

nozzle valve of 0.8 mm diameter orifice, operating at 10Hz. The basic valve design is based on the work of Proch and Trickl [6] with a modification similar to Liu and co-workers [7] and Wodtke *et al*. [8]. The under-study molecules are seeded in He (stagnation pressure of $P_0$=1 bar). The molecular beam is formed by supersonic expansion into the source vacuum chamber. A skimmer (Beam Dynamics) with diameter of 1.5 mm is placed 1-2 cm away from the nozzle orifice in order to select the colder part of the molecular beam. The skimmer orifice is the differential pumping point between the source and detector chambers.

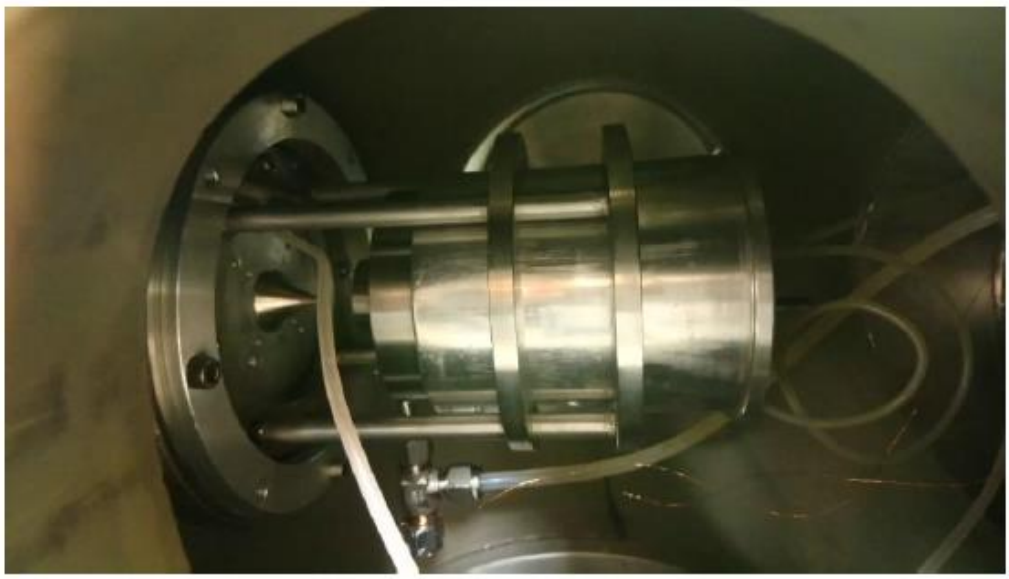

***Figure 2.4: Photograph of the nozzle and the skimmer configuration used.***

## 2.3 Laser Systems

Laser radiation is generated by two pulsed laser systems operating at a repetition rate of 10Hz. The first, is a master oscillator-power oscillator system (Spectra Physics MOPO, 730D10) pumped by a 355nm $Nd^{3+}$:YAG (Spectra Physics, model Quanta Ray Pro 250). The second is an excimer-pumped (Lambda Physik LPX300, operating with XeCl) pulsed-dye laser (Lamda Physik LPD3000). What both these lasers have in common is that they are easily tunable over a wide range of wavelengths (220-900nm for the dye, 220-1800 nm for the MOPO).

In dye lasers, the lasing medium is organic dyes [9]. Typical dye laser design has two stages: oscillator, where the roughly 10% of the excimer laser light excites the molecules of the dye into a state where they undergo stimulated emission and a specific wavelength is picked in a grating-mirror cavity and amplifier where the oscillator output is used as a seeder causing further stimulated emission in a dye solution pumped again by excimer photons (the other 90%). Advantages of the liquid dyes are their high gain as organic dyes in general have very high fluorescence efficiency.

On the other hand, a MOPO system is based on solid state crystals. Their gain comes from the nonlinear frequency conversion process rather than by stimulated emission. In MOPO, the energy contained in a pump photon (produced by an Nd:YAG laser system) at frequency $\omega_p$ is transferred to two other photons $\omega_s$ (the signal wave) and $\omega_i$ (the idler wave) so that to satisfy energy conservation. A parametric gain medium (BBO crystal) is placed in an appropriate resonant cavity for acquiring oscillation at the signal and/or idler wavelength. Typically the pump wavelength of 355 nm is used. No signal input wave is required since the gain in such a system can be large enough and it's created from quantum noise in the crystal. Nevertheless, the output of a MOPO is very similar to that of a laser. The signal and idler beams exhibit strong coherence, are highly monochromatic, and have a spectrum consisting of one or more longitudinal modes.

In order to produce circularly polarized light, a tunable waveplate with freely adjustable phase retardation is used (Alphalas). To set it up, a mirror and a linear polarizer are used to adjust phase retardation to λ/4 as shown in Fig. 2.5.

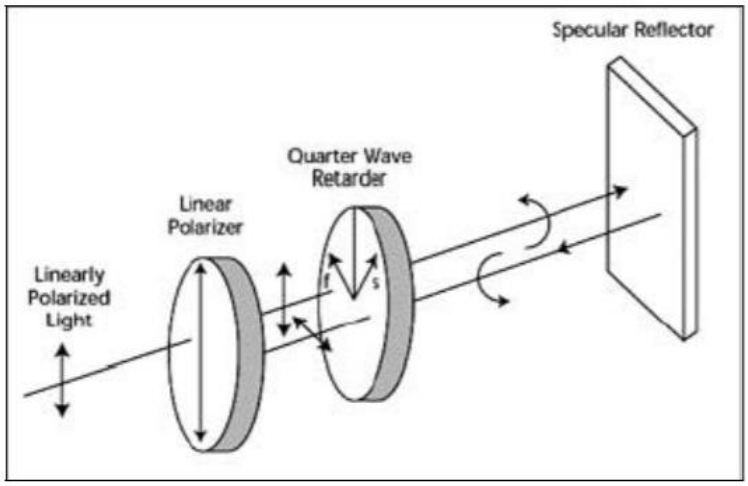


***Figure 2.5: Demonstration of producing circularly polarized light.[10]***

## 2.4 Electrostatic optics and Time-of-flight

The electrons (or ions) produced in our experiments are projected towards the detector by a single-electrode electric field setup, composed by a repeller and a ground electrode (Fig. 2.6). In electron detection mode, the repeller is negatively charged (typically -3kV) and ground electrode is grounded (0V). This combination pushes the electron sphere towards the detector. The extrusions in the repeller and ground electrodes work as an electrostatic lens, similar to the one used by Parker & Eppink for VMI. However, our setup used geometric focusing: laser beam is placed at a specific position between repeller and ground in order for the electrons to be focused on the detector [11]. From the ground electrode to the detector, the electrons fly through a field-free space of ~45 cm. In this region positive or negative ions are separated by mass-to-charge ratio before being detected (time-of-flight separation). This region separates electrons from other negatively charged species. No other such species were detected in our experiments.

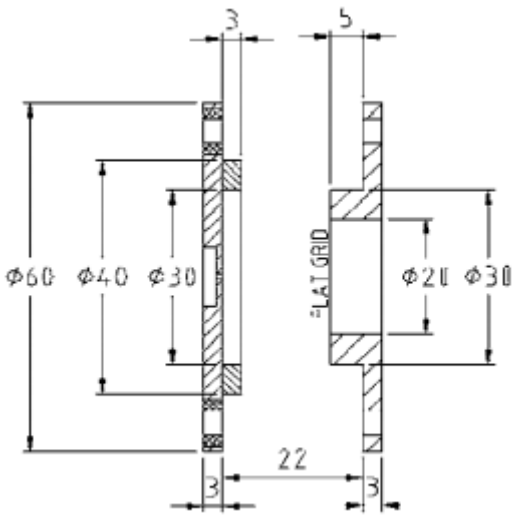


***Figure 2.6: Schematic representation the repeller (left) and ground (right) electrodes in our instrument.***

For the sake of completeness we discuss how time-of-flight separation works. During an experiment, ion formation takes place between the repeller (first electrode) and the ground (second electrode). Afterwards, each ion (electron in our case), with mass m and total charge $q = ez$, is accelerated out of the source region towards the detector due to a potential difference V, the distance between the two plates is denoted as d.
The electric potential energy is converted to kinetic energy and the following equation stands.

$$E_{el} = E_k,$$

$$\frac{zeV}{d} = \frac{qV}{d} = \frac{1}{2}mu^2 \tag{2.1}$$

Here masses start halfway into the field so d≡d/2.
Thus, all the ions with the same charge acquire the same kinetic energy. Following their acceleration, the ions move in a field-free region towards the detector. They reach the detector in time t that can be calculated from the following equation:

$$t_{TOF} = \frac{D}{v} \tag{2.2}$$

Where D is the field-free region and v is their lab velocity along the TOF axis. From the beforementioned relations, one can express TOF time as a function of m/z ratio:

$$\frac{\sqrt{m}}{\sqrt{z}} = \frac{\sqrt{2eV}}{D} t_{TOF} \tag{2.3}$$

## 2.5 Detector

The homebuilt imaging detector located at the end of the detector region (and the end of the time-of-flight path) is comprised of two micro-channel plates (MCPs, BASPIK) coupled to a phosphor anode (P47, Proxitronix) of an effective 50mm diameter. The front face of the MCP sandwich (the side that electrons hit) is grounded and the back one is at +1600V for electron mode operation. MCPs work as a signal amplifier: ~$10^6$ secondary electrons are emitted by the MCP for each electron hitting it. These electrons hit the phosphor screen (held at +6kV) and the photons emitted are recorded by a CCD camera. A pulse generator (Berkley Nucleonics, model BCN 565) is used to control the relative time delays for laser and molecular beam. The experimental parameters are optimized by monitoring the ion or electron signals in a 100Mhz oscilloscope (Hameg HM1007). The raw images are recorded asynchronously every second, ≈ 10 laser shots, by a CCD camera (Unibrain i702b), equipped with a lens with zoom 50mm fl.4 and are saved in the computer. Several thousands of frames are averaged to form images. Each image is further analyzed to extract the speed and angular distribution. Background images are obtained by turning the molecular beam off while keeping all the other conditions unchanged. These images are subtracted from the signal images to get the final raw image and reduce the noise.

## 2.6 Velocity Map Imaging (VMI)

The molecular beam has a finite width on the order of few millimeters so the "focusing" part is of great significance. Prior to analyzing the information we get from the images, it is important to make perfectly clear the physics that lead to them as demonstrated in Figure 2.7

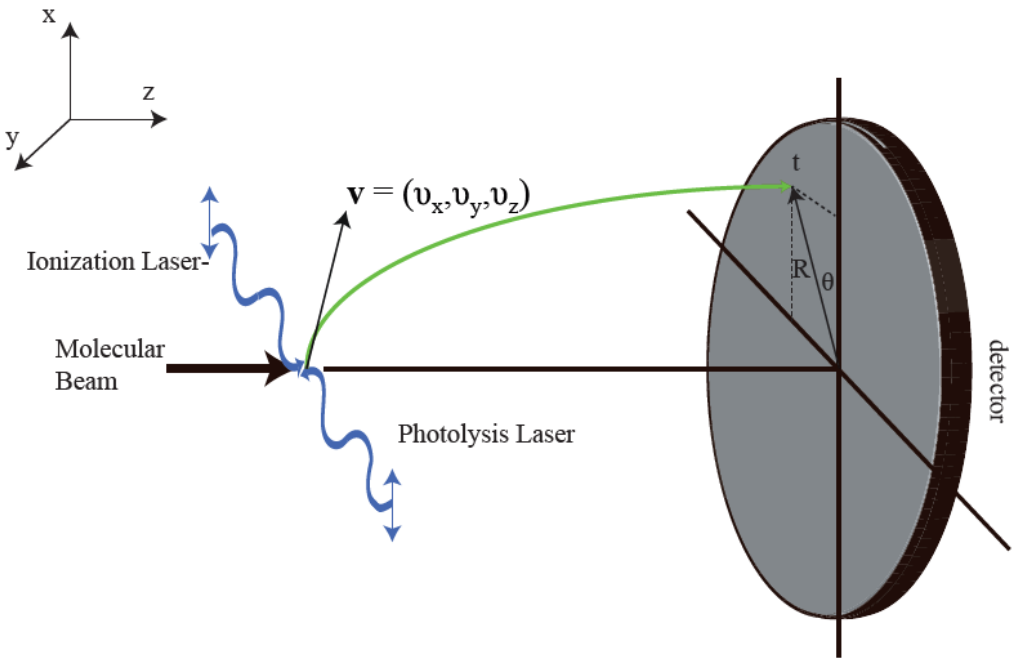


***Figure 2.7: General Scheme of velocity map imaging setup.***

The primary idea is that if the charged particles are formed in an electric field or the field is switched on at the right moment of time, they get accelerated towards the detector in such a way that their arrival positions and times depend on the initial velocities:

$$(\upsilon_x, \upsilon_y, \upsilon_z) \rightarrow (x,y,z) \qquad (2.4)$$

Consequently, it is feasible to determine the initial velocity vector of the particle by using a position-sensitive detector (PSD) and measuring the event position on the detector $\upsilon_x$,$\upsilon_y$ and the time of flight $\upsilon_z$. The electric field is shaped in such a way that the initial positions of the particles do not affect the velocity mapping. This is achieved by introducing inhomogeneity in the extraction field that acts as an electrostatic lens because it focuses the particles velocities onto the imaging plane. The size of the projected sphere (ring) is proportional to the size of the initial Newton sphere. The proportionality constant depends on the repeller voltage used (for a given setup geometry) and is obtained by measuring a particle (ion or electron) distribution of known kinetic energy).

## 2.7 Kinetic Energy Release

In general, the VMI technique is used to study dissociation of molecules. From the recorded images of the photofragments one can extract information on their kinetic energy. A laser photodissociates the target molecule AB in the molecular beam and atomic or molecular photofragments A, B are produced:

$$AB+nhv \rightarrow AB* \rightarrow A+B \quad (2.4)$$

The reactant molecule is prepared in its ground electronic state (or at least in a state that is known for all the molecules in the sample before dissociation), hence, the states of the product fragments can be deduced through conservation of energy:

$$TKER=T_A+T_B= nhv- D_o(AB) - E_{int}(A) - E_{int}(B) \quad (2.5)$$

where hv the photon energy, n the number of photons, $D_o$ the bond dissociation energy and $E_{int}$ each fragment's internal energy (electronic or rovibrational).
The laser-molecular beam interaction point defines the origin of the photofragments. Working in the center of mass frame, momentum conservation, (in the simplest case where AB thermal motion is neglected), dictates the following equation (where $u_A$ and $u_B$ are vectors):

$$m_A\boldsymbol{u_A}+m_B\boldsymbol{u_B}=m_{AB}\boldsymbol{u_{AB}}=0 \quad (2.6)$$

The following relationship about each photofragment's translational energy can be derived from Eq. (2.6):

$$T_A=\frac{m_B}{M}TKER \text{ and } T_B=\frac{m_A}{M}TKER \quad (2.7)$$
$$where, M= m_A+ m_B, \; T_A = \frac{1}{2}m_A u_A^2 \text{ and } T_B =\frac{1}{2}m_B u_B^2$$

Thus, from Eqs. 2.5 and 2.7, we conclude that if fragment A is produced in a known quantum state and we measure its kinetic energy $T_A$ we can calculate the kinetic energy ($T_B$) and internal energy $E_{int}$(B) of its counterfragment B. Imaging all quantum states of A provides info on all states of their counterfragments B.
It is also important to note that fragments A of the same quantum state have the same kinetic energy release $T_A=\frac{1}{2}m_A u_A^2$, therefore at any given time t after the photolysis they will lay on the surface of a sphere of radius $r=u_A*t$, where $u_A$ is the center of mass velocity that A obtained from the photolysis event. This sphere is known as Newton sphere. Fragments A of a different quantum state will be on another Newton sphere with different radius but with the same center (concentric Newton spheres). The center of the Newton spheres is the area in space where the laser photolyzed the parent molecule A-B.
Newton sphere characteristics such as size and surface ion distribution pattern, provide valuable information regarding the dissociation process. The size of the Newton sphere is directly proportional to the fragment's speed (scalar quantity).

In this work we focus on the photoelectrons. A laser ionizes the molecule A in the molecular beam and an electron is extracted (in reality more than one electron are extracted but we do that for simplification) so Eq. 2.4 becomes:

$$A+nhv \rightarrow A* \rightarrow A^+ + e^- \quad (2.8)$$

Respectively to the previous analysis, considering energy conservation, the total kinetic energy release (TKER) of the electron and the anion will be equal to:

$$\text{TKER}= T_A+T_e= nhv- \text{IE}(A)-E_{int}(A^+) \quad (2.9)$$

where IE is the ionization energy of A.
From momentum conservation, Eq. 2.7 becomes

$$T_A=\frac{m_e}{M}TKER \; and \; T_e=\frac{m_A}{M}TKER \qquad (2.10)$$
$$where \; M= m_A+ m_e, \; T_A = \frac{1}{2}m_A u_A^2 \; and \; T_e=\frac{1}{2}m_e u_e^2$$

Since the mass of the electron is a lot less than the mass of the molecule, we can assume that the electron ends up with the total kinetic energy**.**

$$T_e= nhv- \mathrm{IE}(A)-E_{int}(A^+) \qquad (2.11)$$

## 2.8 Angular Distributions

The distribution of photofragments on the Newton sphere will be isotropic if molecules are randomly oriented in space (i.e. not preferentially aligned in one or another direction) and they are photolyzed with equal probability. The latter is determined by the absorption probability of a laser photon by a randomly oriented molecule.
The probability of absorption for an electric dipole transition is given by [12]:

$$P_{abs} \propto cos^2\theta \qquad (2.8)$$

where θ is the angle between the transition dipole moment μ and the electric vector E of the photolysis laser.
As the transition dipole moment μ is always parallel to the electric field, if a linearly polarized laser is used, parent molecules whose internuclear axis is parallel to the electric vector will be preferentially excited creating a preferential orientation in space of the resulting photoproducts in a $\cos^2\theta$ distribution. This is the case only when the recoil time of the fragments is short compared to the parent molecule's rotational period and there is no substantial delay between the moment of the optical excitation and the bond rupture. This type of transition is described as parallel. Likewise, a perpendicular transition would yield a $\sin^2\theta$ distribution.
If the transition moment is not oriented in a parallel or perpendicular manner to the molecular axis, then it displays a mixture of parallel and perpendicular character. Same result can be obtained in the cases where the dissociation is slow compared to the parent's rotational period (predissociation): thereafter the resulting angular distribution will deviate from the parallel/perpendicular limits. For photoelectrons, a similar analysis applies to angular distribution; however, as we discussed in Chapter 1, in PECD it is the odd terms in the angular distribution according to dipole approximation that give rise to the measured forward-backward asymmetry.

References

[1] A. T. J. B. Eppink and D. H. Parker, Review of Scientific Instruments 68, **1997**, 3477.
[2] Building Scientific Apparatus, J. H. Moore, C. C. Davis, M. A. Coplan, Cambridge University Press, **2009**, Fourth Edition.
[3] Kurt J. Lesker Company.
[4] J. J. H. van den Biesen, In Atomic and Molecular Beam Methods, Vol. I, ed. G. Scoles, (Oxford University Press, New York, **1988**) p472.
[5] G. Scoles, Atomic and molecular beam methods, **1988**, New York: Oxford University Press.
[6] D. Proch and T. Trickl, Review of Scientific Instruments, **1989**, 60(4), 713-716.
[7] F. Dong, S.-H. Lee, and K. Liu, J. Chem. Phys. **2000**, 113, 3633.
[8] Q. Ran, D. Matsiev, D. J. Auerbach, and A. M. Wodtke, Rev. Sci. Instrum.**2007**, 78, 104.
[9] Schäfer F.P., Principles of Dye Laser Operation. In: Schäfer F.P. (eds) Dye Lasers. Topics in Applied Physics, vol 1. Springer, Berlin, Heidelberg, **1973.**
[10] Basic Polarization Techniques and Devices, **2005**, Meadowlark Optics, Inc.
[11] V. Papadakis and T. N. Kitsopoulos, Rev.Sci. Instrum. 77, 083101, **2006**.
[12] R. N. Zare. Photoejection dynamics. Mol. Photochem., 4:1, 3, **1972**.

# Chapter 3-Development of a sample heater for a piezoelectrically-actuated nozzle

## 3.1 Previous work on heating systems

It's not peculiar to think that a large number of gas phase experiments require the heating of the samples because they may not have high vapor pressure.
Many chiral species of interest are of low volatility (glycine, alanine, valine etc [1]), they are not gaseous at room temperature, so they need to be vaporized. In particular, biomolecules are often thermolabile which led to the creation of sophisticated techniques to propagate fragile molecules efficiently to the gas phase, such as aerosol thermodesorption (TD) and resistive heating (RH). Aerosol sources make use of a thermal desorption step when aerosol particles of nanometric size, consisting of the pure substance under study, impinge on a heat [2]. Thermodesorption [3],[4] happens on a hot tip located very close to the ionization volume and it is used for handling thermally unstable molecules. It is a soft vaporization technique producing intact nascent neutral parents but with reduced signal and lowered electron kinetic energy/ion mass resolution.
Resistive heating[8],[9] is performed in an oven prior to adiabatic expansion. It has the drawback of contamination due to unwanted thermal decomposition of the sample, however it is simpler to implement compared to other methods.

For PECD experiments resistive heating has been used [5.6] although in those cases the nozzles were solenoid-based. The nozzle we're using in this project is a piezoelectrically actuated one. That means that we can't heat the sample area and the whole nozzle at the same time, because the piezo crystal withstands up to 100°C. Therefore, we had to develop a system that would evaporate the under-study molecule without a temperature increase in the crystal region of the nozzle.

## 3.2 Piezoelectrically actuated nozzle design

The nozzle used in this experiment is a home-built piezoelectrically actuated nozzle valve (0.8mm diameter) operating at 10 Hz. The basic valve design is based on original work of Proch and Trickl [7], with a modification similar to work of Liu and co-workers [8] and similarly Wodtke and co-workers [9]. When applying voltage to a piezoelectric crystal, the crystal changes shape slightly. So, when applying pulsed voltage, the crystal's shape changes correspondingly, and with the appropriate adjustments it can close or open the nozzle's orifice and hence produce a pulsed molecular beam exiting the nozzle. Since the whole structure is made of metal, therefore is thermally conductive, there is the risk when heating the sample area, that the crystal is also being heated. This excluded the use of an IR lamp as an option for heating. One possible solution to this problem is to apply resistive heating, using a wire wrapped around the area where the sample is placed. Some criteria that needed to be met for the wire are:

- Flexible enough so that it can be adjusted to the desirable surface
- Material that can be used in vacuum
- Not very thin for endurance in time
- Not very thick in order to optimize the time needed to heat enough to transfer energy to the surface
- Temperature should be increased gradually.

Also, the use of two different thermocouples is necessary for temperature measurements near the heating point and on the nozzle's crystal at the same time. The difficulty in this application is that

whereas the tip of the thermocouples should be in the vacuum chamber and adjusted on the surfaces of interest, the ending of them should connect to the thermometer device which is outside the chamber. The way we managed to meet all those requirements is described in the next section.

## 3.3 Construction

The first thing needed to be done, was to make sure that the temperature in the nozzle wasn't increasing. We noticed that with a short wire, two hours weren't enough to increase the temperature by 5°C, so we used 2m long wire and after 3 hours the temperature was raised more than 20°C whilst the rest of the nozzle just 1°C, by applying current of 1A. The power supply used provides up to 3A current. So, two meters of a Copper-Nickel wire of 0.22 mm diameter varnished with an insulating coating was used for the experiments in atmospheric pressure and the results are shown in Figure 3.1.

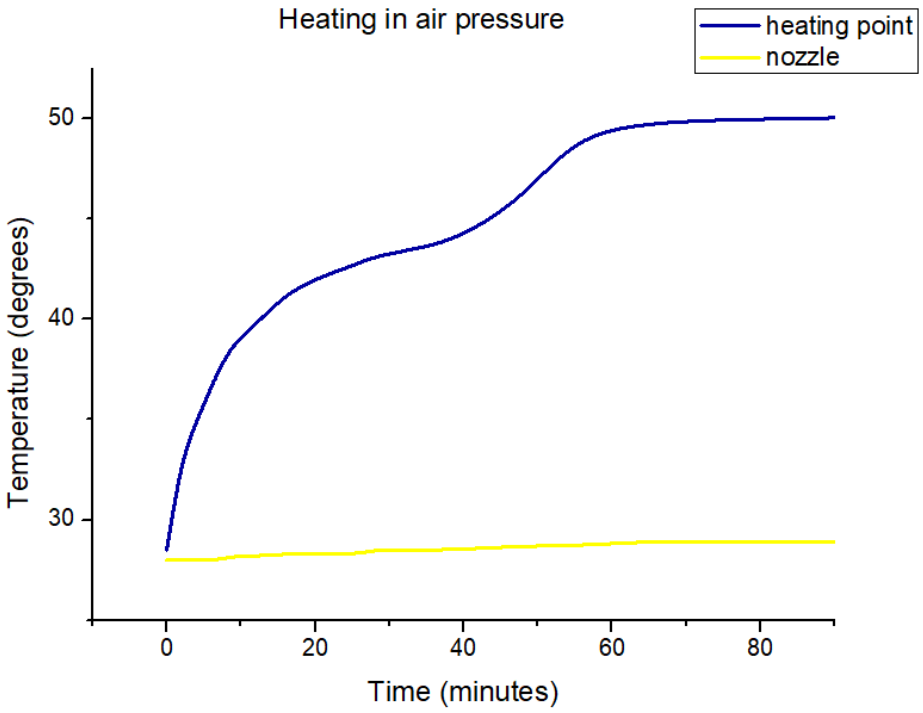


***Figure 3.1: First experiments for heating conducted in air pressure.***

It is evident that while slowly, the temperature is increasing in the heating point (where the sample is placed), the rest of the nozzle conserves its temperature. The system was operating for more than three hours and no difference from the above was observed.

Obviously, the conditions inside the vacuum chamber differ and furthermore the need emerged of finding a way to connect the thermocouples in the chamber, with the thermometer outside this chamber. Thermocouple wires were connected to vacuum feedthroughs on a flange and a simple coaxial wire then connected the feedthrough to the thermometer device. We used K-type (RS) thermocouples since the range of temperatures used were up to 100°C. Each of the two thermocouples used has two wires, nickel and copper. Each copper wire connected to a different feedthrough for each thermocouple, while the two nickel wires (from the two thermocouples) connected, to the same feedthrough. During the setup of these connections, solder was used to make them more stable. Similarly, the heating wire connected to feedthroughs inside the chamber and coaxial cables carried current to these wires from the power supply. At this point we should clarify

that all the connections from the inside of the vacuum chamber to the outside were made with feedthroughs.

A problem that appeared is that we had to keep the tip of the thermocouples in touch with the surfaces we were measuring, however it was tough to keep the tip in contact with the surface measured at all times. The first attempts were with the use of aluminum tape which has glue on one side. The increase of temperature, caused glue destruction and loss of connection to the thermocouple tip (i.e. tape just fell off). The solution to this problem was the use of o-rings. The tips of the thermocouples were tightened on the location of choice with o-rings that have the additional advantage that they are made to work in vacuum.

A few photos from the first test in air and in vacuum are presented in Figure 3.2.

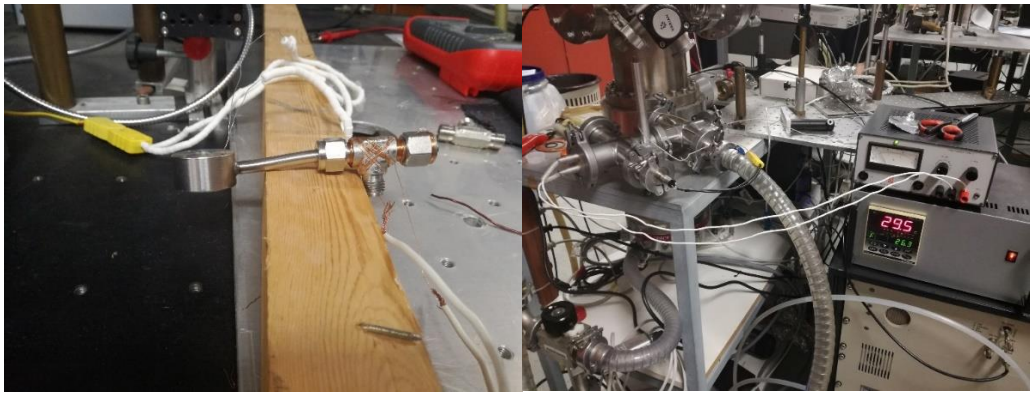


***Figure 3.2: Photos from the first tests in air (a) and in a small vacuum chamber (b).***

In vacuum, the temperature is changing as in Figure 3.3. The main part of the nozzle remains significantly unaffected while the temperature at the heating point increases more than in 1atm since collisions with air molecules are out of the equation. Most importantly, nozzle's performance wasn't affected at all.

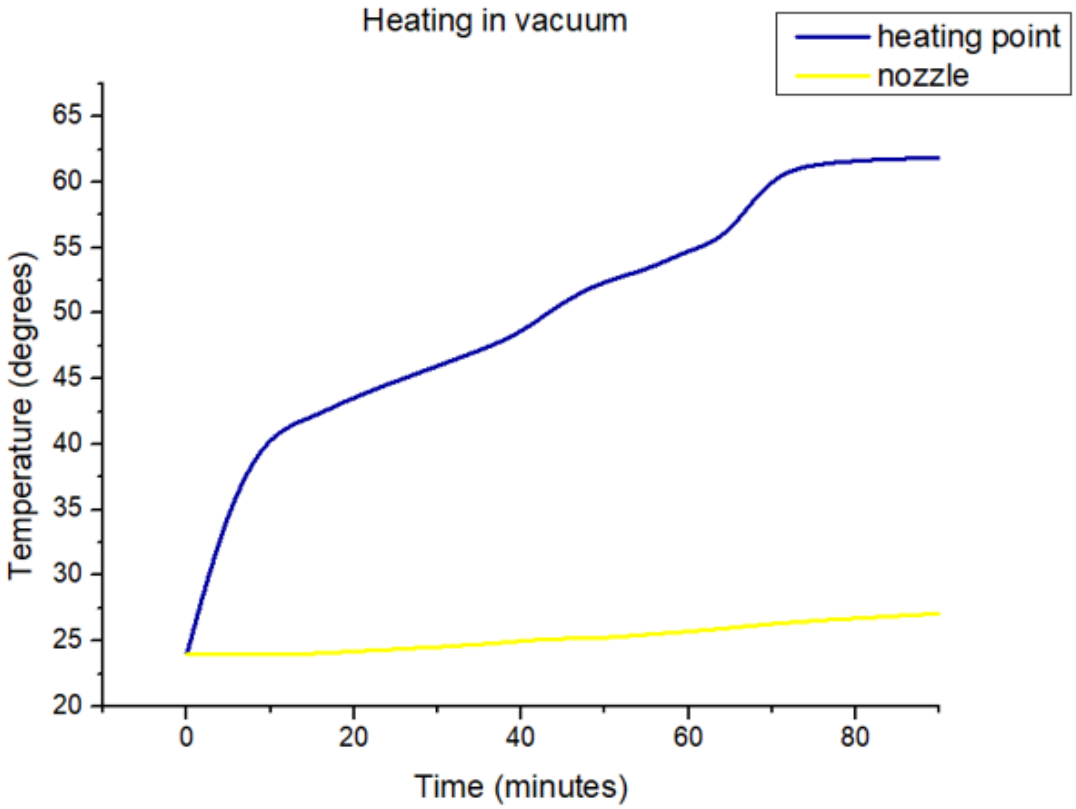


***Figure 3.2: Experiments for heating conducted in vacuum.***

At this point of the construction a problem made its appearance. The heating system was working as well as the thermocouples, but we couldn't see any signal of our chiral molecule. The reason was that because of the arrangement (see Figure 3.2 a) Helium gas wasn't necessarily pushing the molecules through the nozzle so we changed the three-way adapter (union) with an elbow one (two-way), to assure that the gas molecules are drifting along with helium.

After a couple of weeks using these, the varnished coating of the wire used for heating melted and the wire was getting cut from the 80°C that it reached and the lots of hours of work. To prevent this and to make it more endurable, we used heat-shrinkable insulating wire for the heating wire from the flange to the nozzle.

## 3.4 Final heating system and recorded image

The final design that is now operating is depicted in Figures 3.3 and 3.4. In Figure 3.3 we can see the two thermocouples and the way they are connected with the flange via the feedthroughs. Also, we can see the heating wire with the protecting insulation and the place (right angle connector) where the sample is. As He carrier flows through the connector it carries sample molecules towards the nozzle orifice. The nozzle's orifice is 5cm away from the heating point and stays unaffected.

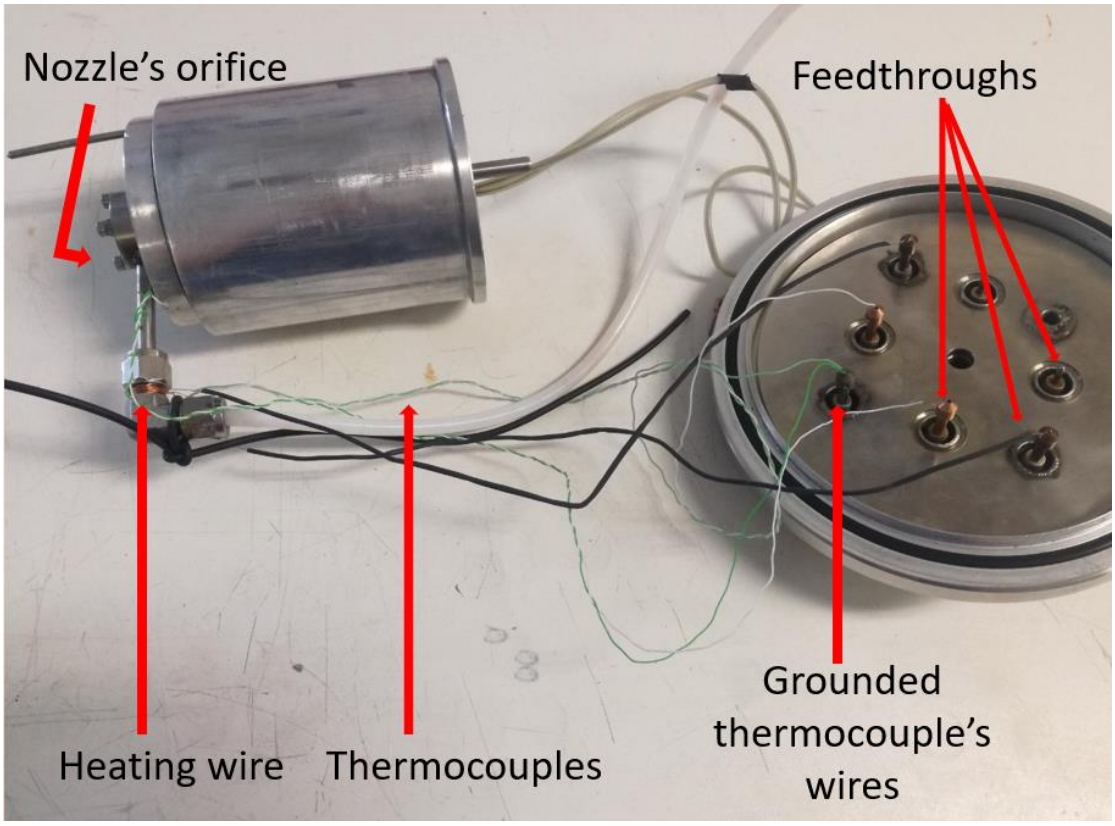


***Figure 3.3: The new heating system and its connections with the feedthroughs.***

In Figure 3.4 is the same set-up from a different angle to make clear the places that we measure the temperature.

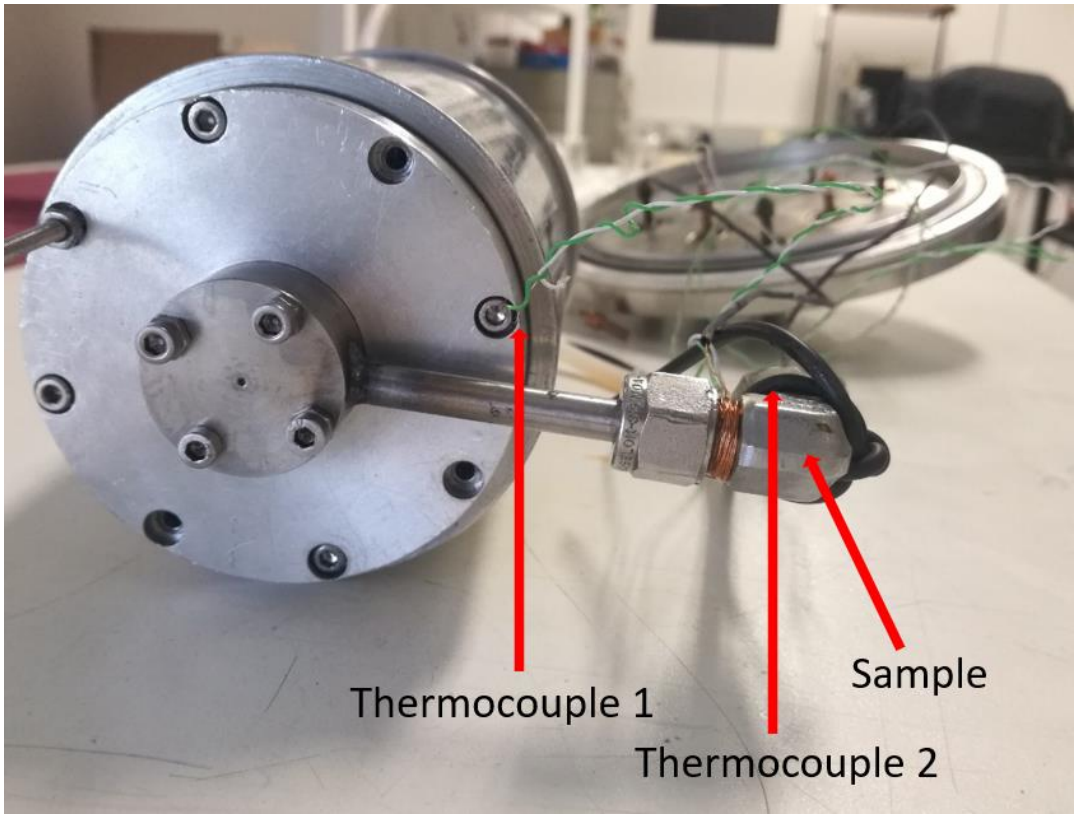


***Figure 3.4: The front of the nozzle, the two thermocouples and the sample area.***

Finally, since all the problems were solved, an image from R-(+)-limonene ionization was recorded (Figure 3.5). This demonstrates that the heated nozzle actually works as intended.

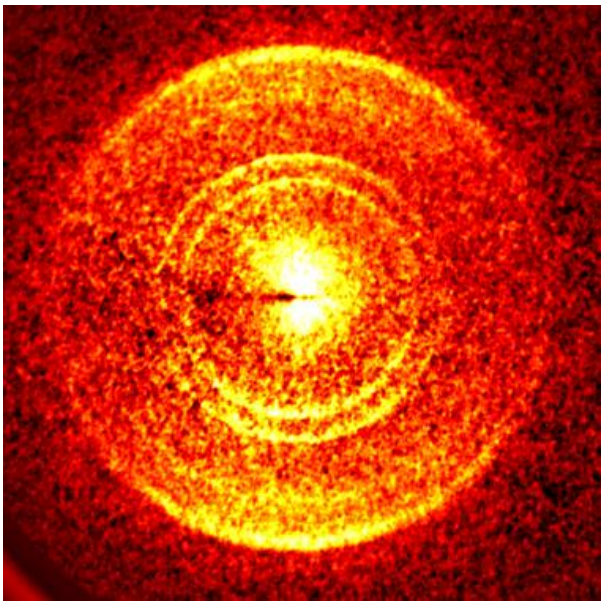

***Figure 3.5: R-(+)-limonene image recorded at 303nm with the new heating system.***

References

[1] M. Meot-Ner *et al.*, Journal of the American Chemical Society, 101:3, 686-689, (**1979**).
[2] V. Touboul *et al.*, The Journal of Chemical Physics, 138, 094203, (**2013**).
[3] F. Gaie-Levrel *et al.*, Phys. Chem. Chem. Phys., 13, 7024-7036, (**2011**).
[4] P. Kaul *et al.*, Journal of Crystal Growth, 123, 411-422 (**1992**).
[5] R. Hadidi*et al.*, Advances in Physics: X, vol 3, No 1, 1477530 (**2018**).
[6] L. Nahon *et al.*, Journal of Electron Spectroscopy and Related Phenomena, 204, 322-334, (**2015**)
[7] D. Proch and T. Trickl, Review of Scientific Instruments, 60(4), 713-716, (**1989**).
[8] F. Dong, S.-H. Lee, and K. Liu, J. Chem. Phys., 113, 3633, (**2000**).
[9] Q. Ran, D. Matsiev, D.J. Auerbach, and A.M. Wodtke, Rev. Sci. Instrum., 26, 12, 1150, (**1955**).

# Chapter 4-Image Analysis

In this chapter, we're going to discuss the data analysis used to extract PECD information from the experimental data. As it has already been described previously, the result of the experiment is an image: a projection of the 3D Newton sphere of the photoelectrons ejected following photoionization of a chiral molecule onto our 2D detector. This "raw" image undergoes inverse Abel transform in order to be able to extract the angular distribution: the number of electrons ejected as a function of solid angle. This work is done by programs developed in our lab, adapting widely available algorithms for image processing and inverse Abel transform implementation. These programs operate in command prompt (DOS) mode.

## 4.1 Converting the image into a .raw file

The custom-made program that grabs images during the experiment outputs them into .img format: 32 bit, 1388x1040 images, with a 512 bytes header (total size of 5.774.592 bytes). In order to inspect the image and further process it, we need to convert it into a format that is both readable by graphics programs such as Adobe Photoshop and easy to open and process with our custom-made analysis programs. The format of choice is the 16 bit ",raw" format. Raw (.raw) images can be opened in Photoshop (size, color depth and header need to be specified) and can also be read by our analysis programs. Besides visualization, when several files under the same conditions are recorded, a need emerges for adding them together to produce a sum image for further processing, or for subtracting background images. Especially in the case of PECD, its quantification requires subtraction of the right-handed circular polarization (RCP) data from the left-handed (LCP) data (or the opposite). The "add32" algorithm/program is used to carry out these additions/subtractions where needed.

The program reads the first .img file specified by the user. Then it prompts the user to add or subtract a file or exit. If exit is chosen, the input 1388x1040x32 bit file is converted into a 1040x1040x16 bit .raw file. The camera is positioned in such a way that the detector occupies only the bottom 1040x1040 square of the 1388x1040 CCD image. Therefore, the top 348 pixels carry no useful information and can be safely deleted to leave the 1040x1040 square output image. In case addition or subtraction is chosen, then user is then prompted for an image file name to be added/subtracted and a scaling factor (i.e. how many times the image file will be added subtracted). Then the addition/subtraction of the file is carried out and the result is kept internally in a real-number matrix. The scaling factor is useful in cases where one background image is taken every two or more images. Decimal (e.g. 0.5) scaling factors are supported. The loop prompting for addition/subtraction/exit is repeated until user chooses "exit". Then the matrix is written in the output file (1040x1040x16 bit .raw file as described above), which can then be easily opened with a graphics editor such as Adobe Photoshop. An example from this work with the right circularly polarized light, the left circularly polarized light and the subtraction of the two is shown in Fig. 4.1.

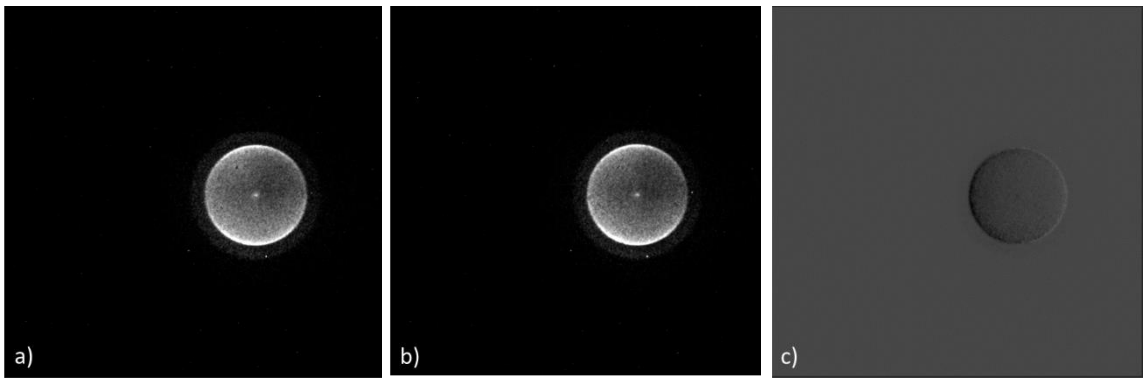


***Figure 4.1: Raw images recorded with a) right circularly polarized light, b) left circularly polarized light and c) subtraction of right circularly polarized light from left circularly polarized light at 377nm for fenchone.***

## 4.2 Specifying the center

It is apparent from Fig. 1 that the center and the radius of the disc should be determined. The first is feasible with the use of two programs. The first adds pixel intensities in a user-specified range of rows and outputs a histogram of intensity vs column. The second adds pixel intensities in a user-specified range of columns and outputs a histogram of intensity vs rows. Typically, ranges of 10 pixels are used. Figures 4.2 and 4.3 illustrate how this works.

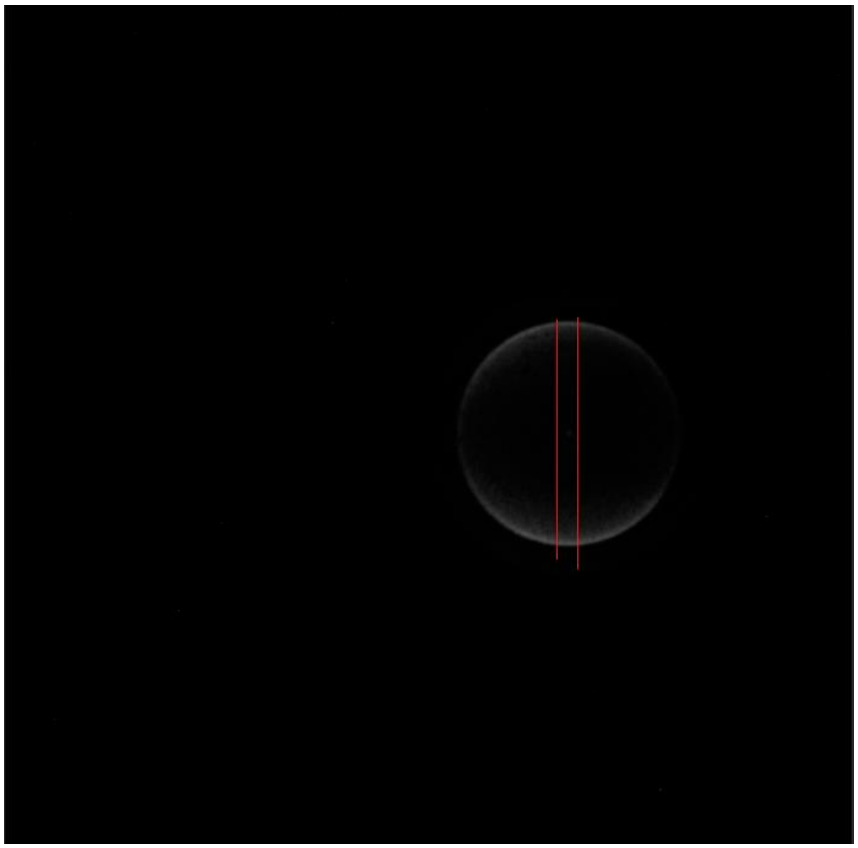

***Figure 4.2: A .raw image of linearly polarized light at 377nm for fenchone. The red lines show potential limits.***

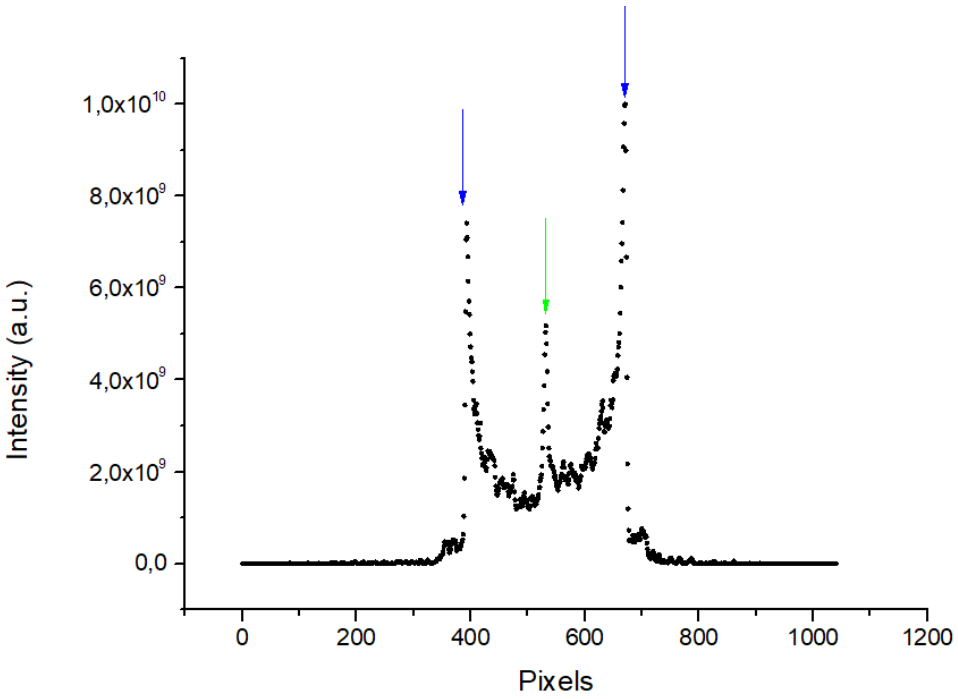


***Figure 4.3: The graph shows Intensity vs pixel for the image in Fig. 4.2. The blue arrows correspond to the top and the bottom parts of the disc and the green to the center.***

It is now evident the way that we're able to determine with accuracy the position of the center.

## 4.3 Inverse Abel Transform

Inverse Abel transform is used to reconstruct the full three-dimensional distribution from the recorded two-dimensional projection of the charged particles. This transform has the necessity of cylindrical symmetry parallel to the imaging plane so we need to modify the images according to whether they are from linear polarization or circular, so that the transform can be applied correctly. Inverse Abel transform is used to calculate the emission function given a projection of that emission function [1].The input to the reconstruction method is each row of pixels that corresponds to two-dimensional ring distributions. The result is a slice through the center of the original three-dimensional distribution, which is the reconstructed image and is a sum of concentric rings corresponding to each crushed Newton sphere. The reconstructed images are enclosing a large amount of information and their properties, e.g. its radius, angle and intensity. The program performs the transform by taking a Fourier transform followed by a Hankel transform.

## 4.4 Speed Distribution

As it has already been mentioned, the radial position is a direct measurement of the ions' kinetic energy. The program opens the image file and uses only half of the image, the right part. The output is an integrated intensity as a function of the radius. This integration occurs between 0 and 180 degrees and weights the intensity of each pixel by sin(theta) to get the "total 3-D translational energy distribution". During the execution, we need to provide the maximum radius, which is the maximum radius of the disc, and the center of mass position, which is the center of the disc that has already been calculated. The second, is used as a shift so that it corresponds to zero and all the other quantities are measured regarding to that. Granted that the integration happens over radius, there's the need for converting the coordinates to polar which we do while applying the shift for the center

of mass and then use the converting equations:

$$r = \sqrt{x^2 + y^2} \tag{4.1}$$

$$\varphi = \text{acos}(\frac{y_i - i}{r}) \tag{4.2}$$

Where x,y are the cartesian coordinates of each pixel after the center of mass shift has been taken into account, $y_i$ is the y coordinate of the center of mass position, i the x coordinate of each pixel without the subtraction of the shift and r and φare the radial and angular coordinates respectively. After the verification that the radius is within selected limits, the integration is performed and the output is a .dat file which is easy to plot. A typical graph from this part is presented in Fig. 4.4.

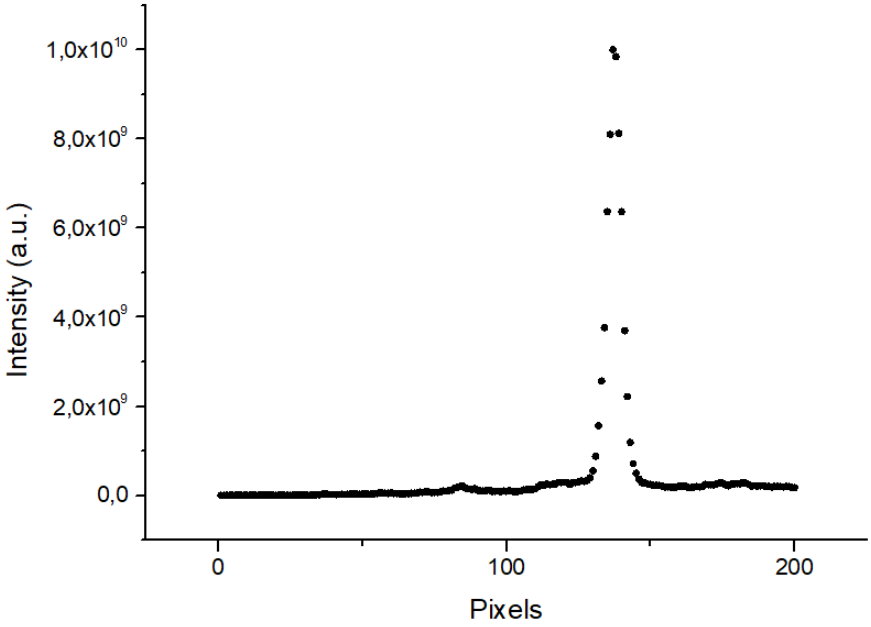


***Figure 4.4: A typical graph of intensity over pixels.***

It's easy to convert the pixels into energy since we know that the pixel position is proportional to $\sqrt{E_{kin}}$ thus we can relate the kinetic energy with pixels as follows:

$$E = K_{cal} * \text{pixel}^2 \tag{4.3}$$

In this equation $K_{cal}$ is a calibration factor weighting for experimental parameters like repeller voltage and spatial position of the photolysis laser. Energy units are arbitrary. This calibration factor can be determined experimentally using a well-known photodissociation process.

## 4.5 Angular Distribution

Likewise, the surface pattern (angular distribution) of the ions is obtained by integrating the symmetrized image from the center over a defined maximum radius from 0° to 180°. The recorded images for linear polarization are edited with a program that assumes only half of the image – the right side. The first thing that the program does is check that the size of the image is within the

limits. Afterwards, we need to input the minimum and maximum radius, in other words, the limits of the well-defined under-study ring of the disc. In order to do that as accurately as possible, we open the graph from the previous part (speed distribution) and before converting into energy, we choose the limits in pixels and directly use them in the program. Then you choose the angle step size that the integration is going to be performed. Usually we choose 5 degrees. As before, we insert the coordinates of the center of mass and convert the images' information again to polar coordinates. We check whether the radius is within the selected limits and the x value is within the selected window and if so, this value is added to the sum of the integration. Finally, the intensity is normalized to the number of pixels in the under-integration area. Figure 4.5 contributes to the visualization of this procedure. On the left is the image experimentally recorded, and on the right the red circles show the radius limits that we choose so that integration is executed only within those limits.

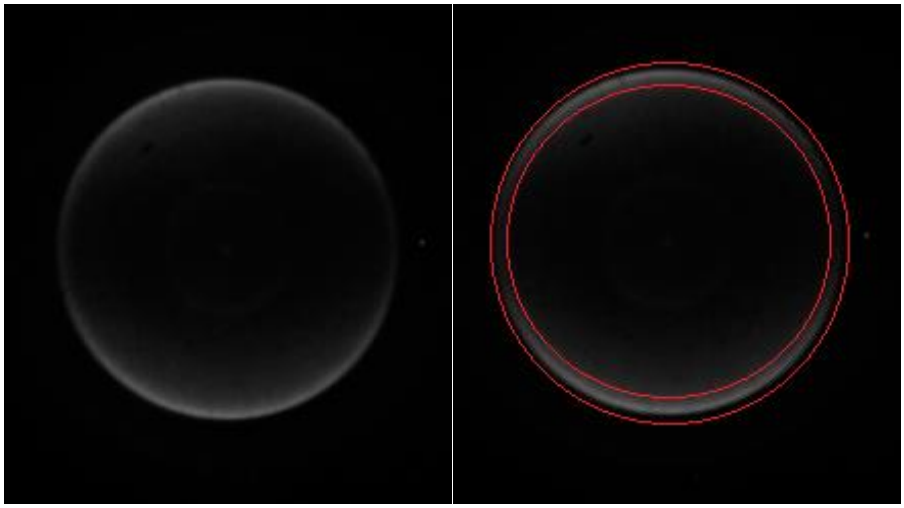

***Figure 4.5: A raw image for linear polarization on s-fenchone at 413.580nm. Both images show the same file with the difference that on the right red rings there have been added to visualize the radius limits that are imported in the program.***

The output of this program is a dat file that we plot and fit with the Legendre polynomials to determine the $b_2$, $b_4$, … coefficients as described in Chapter 1.

The reader can easily note that as useful as this program is for linear polarization, it can add nothing to the PECD signal since we want to proceed on the whole image because of the difference on the right and left part of the disc. For that reason, a few modifications were made to the program to be able to integrate over 360°. After the conversion to polar coordinates and to radians, there is a logical expression, so if the value of the radius is greater than the minimum value of radius we have already imported and if it's less than the maximum radius respectively and also if the value of the angle is greater or equal to the value that is integrated(theta) and less or equal to theta plus the step that we have chosen, then this intensity value is added to the sum. The final step is to normalize and the output is a dat file that when plotted corresponds to the intensity over angle from 0° to 360°. In Fig. 4.6 we can see a raw file after the subtraction of the right handed circular polarization from the left handed circular polarization and the difference of the right part from the left part of the disc is evident.

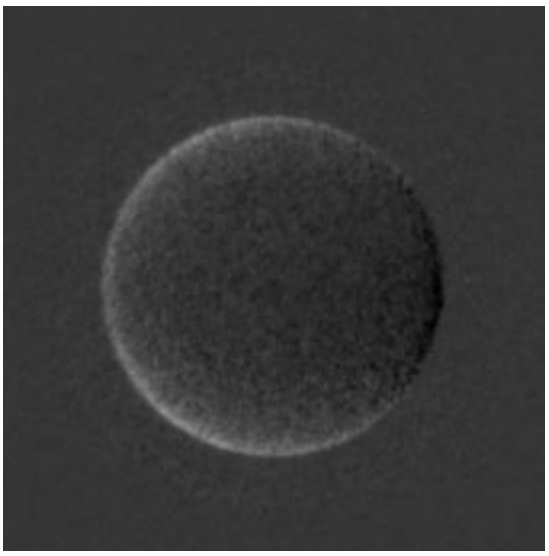

***Figure 4.6: A raw image after the subtraction of RCP to LCP on s-fenchone a***

References

[1] N. H. Abel, Journal für die reine und angewandte Mathematik, 1, **1826**, 153-157.

# Chapter 5-Fenchone

## 5.1 Introduction

Photoelectron circular dichroism, as has already been described in chapter 1, is a highly sensitive enantiospecific spectroscopy for studying chiral molecules in the gas phase. The first PECD measurements were conducted on camphor in both the VUV (valence) [1],[2],[3] and soft X-ray (C 1s) [4]regions. Since fenchone is a closely related molecule to camphor, it was the second chiral molecule that was studied**.** These two species are structurally similar and just differ in the site of attachment of two methyl groups, that's the reason their comparison has attracted such attention [5,6,7,8,9,10,11].

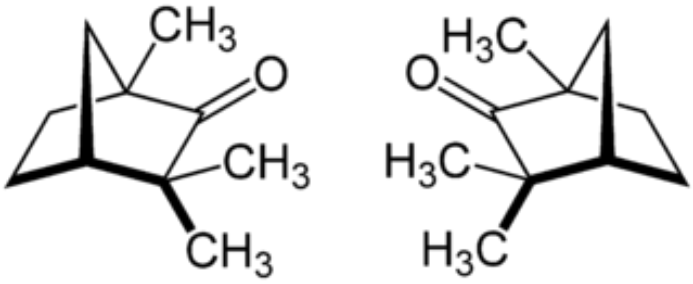


***Figure 5.1: Structure of the two enantiomers of fenchone molecule.***

The first experiments were conducted using synchrotron radiation whose tunability and stability provides an in-depth study on the dynamic richness of this effect [11,12]. However, its long duration prevents ultrafast dynamical studies. Afterwards, they measured the ultrafast dynamics of fenchone using different light sources from the extreme ultraviolet to the mid-infrared range, leading to different ionization regimes: single-photon[13], resonance-enhanced multiphoton [12,14,15], above-threshold and tunnel ionization[16]. These results using femtosecond laser radiation led Wollenhaupt to conclude that the PECD is universal with the sense that the molecular chirality is encoded in the photoelectron angular distribution (PAD) independent of the ionization regime [4,17]. Other attempts in fenchone revealed the possibility of observing PECD from excited states, for instance loosely bound electronic states, via a pump-probe technique that provides time-resolved signal (TR-PECD) [18]. Moreover, Kastner et al. manufactured a prototype that after the measurements and analyzes of the PAD from randomly oriented fenchone molecules in the gas phase they found a dependence with respect to the enantiomeric excess (ee) values to below one percent by using femtosecond PECD[19]. The same group proved intermediate state dependence of PECD in resonance-enhanced multi-photon ionization of fenchone and observed a sign change in the signal depending on which electronic state is used as an intermediate, so they were able to identify two differently behaving contributions [20]. Lately, they have even related PECD signal with a photophysical astrophysical scenario for the origin of life's homochirality [21] and extensive work has been done on the generalized perspective on chiral measurements without magnetic interactions [22] and on the physical mechanism underlying this asymmetric electron ejection [23].

A breakthrough was made recently when PECD was observed using an ultra-violet nanosecond pulse to ionize chiral showcase fenchone molecules [24]. They found that compared to femtosecond ionization, the magnitude of PECD is similar, but the lifetime of intermediate molecular states imprints itself in the photoelectron spectra. By comparing their results to the ones from fs findings on the same molecule they discovered that the 3s state dominates the PES for the ns experiment attributed to its longer lifetime as compared to the 3p

state. The observed PECD value for the 3s state is in agreement with the previous fs PECD values.

## 5.2 Results and Discussion

Our work has been focused on multiphoton PECD on fenchone, obtained by high-resolution 2+1 (2 photons to reach the electronic state and 1 to ionize the molecule) resonance enhanced multi-photon ionization (REMPI) via the 3s Rydberg state with a nanosecond pulsed dye laser (described in section 2.3). The wavelengths of the radiation used are from 375nm to 420nm for the 3s state. The enantiopure s-(+)- and r-(-)-fenchone samples were purchased from Sigma-Aldrich and used without further purification. The enantiomeric excess, which is a measurement for purity for chiral substances with 100% being the completely pure enantiomer and 0% reflecting a racemic mixture, as measured by gas chromatography was 99.9% for s-(+)-fenchone and 84% for r-(-)-fenchone[25].

First, in Figure 5.2 we show the two raw images obtained for right and left circularly polarized light**.** It's obvious that there are not significant differences between the two images in the angular distribution.

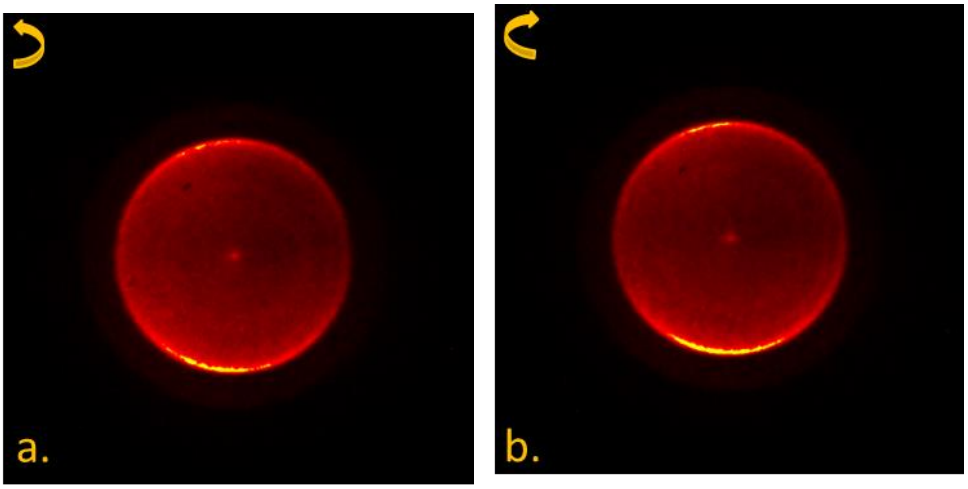


***Figure 5.2: PADs for s-(+)-fenchone ionized via 2+1 REMPI using 388nm (a) left and (b) right circularly polarized light. The arrows indicate the polarization.***

In Figure 5.3 there are two raw images showing the photoelectron angular distribution (PAD) obtained using (a) linear polarization and (b) the subtraction of right-handed circularly polarized light from left-handed circularly polarized light.

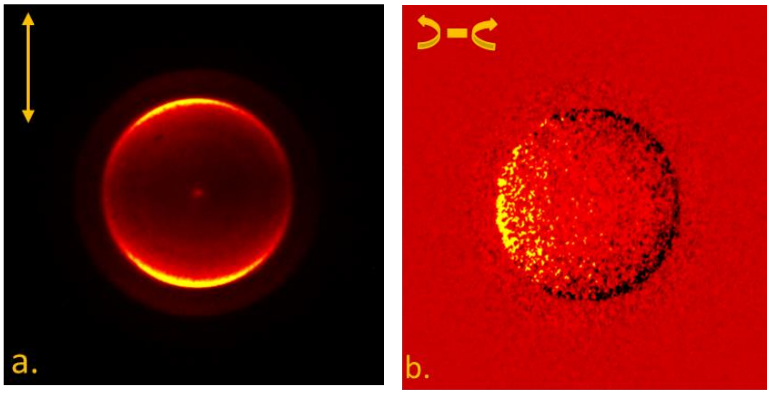


***Figure 5.3: PADs for s-(+)-fenchone ionized via 2+1 REMPI using 388nm (a) linearly and (b)circularly polarized light. The arrows indicate the polarization.***

We observe a distinct forward-backward asymmetry of the emitted photoelectrons with respect to the propagation axis of light in(5.3 b) which is not in the corresponding linear (5.3 a). Figure 5.4 shows recorded images for several wavelengths where the differences in angular distribution are evident.

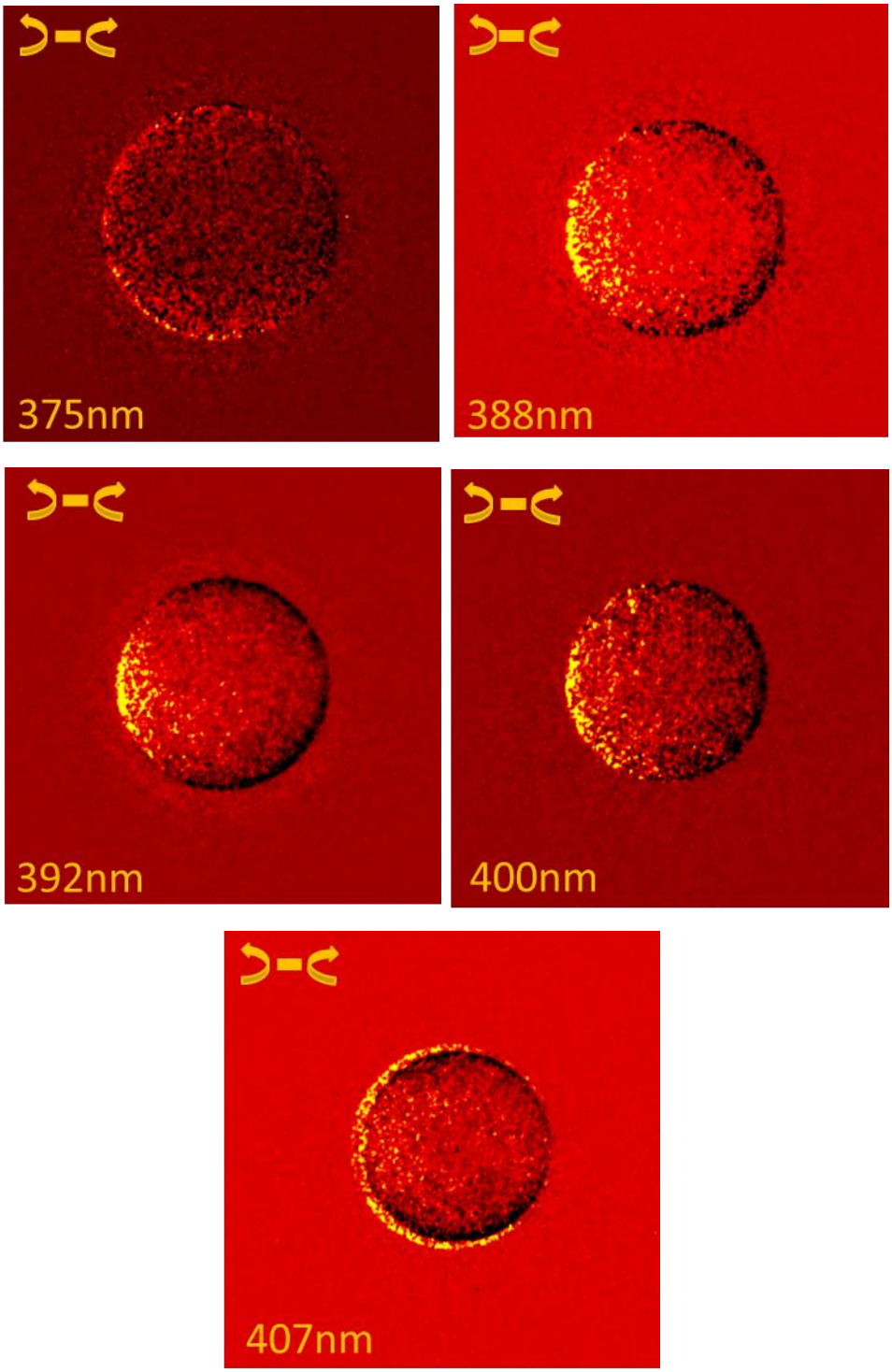


***Figure 5.3: PADs for s-(+)-fenchone ionized via 2+1 REMPI using different wavelengths.***

A few indicative experimental data for angular distribution for the linear polarization as well as the corresponding fittings (red line) for the intensity are presented in Figure 5.4. We recall the relationship for the intensity for linear polarization:

$$I_0(\theta) = 1 + b_2^{\{0\}} P_2(cos\theta) + b_4^{\{0\}} P_4(cos\theta)$$

As we have already explained from these fittings we get the values for $b_2$ and $b_4$.

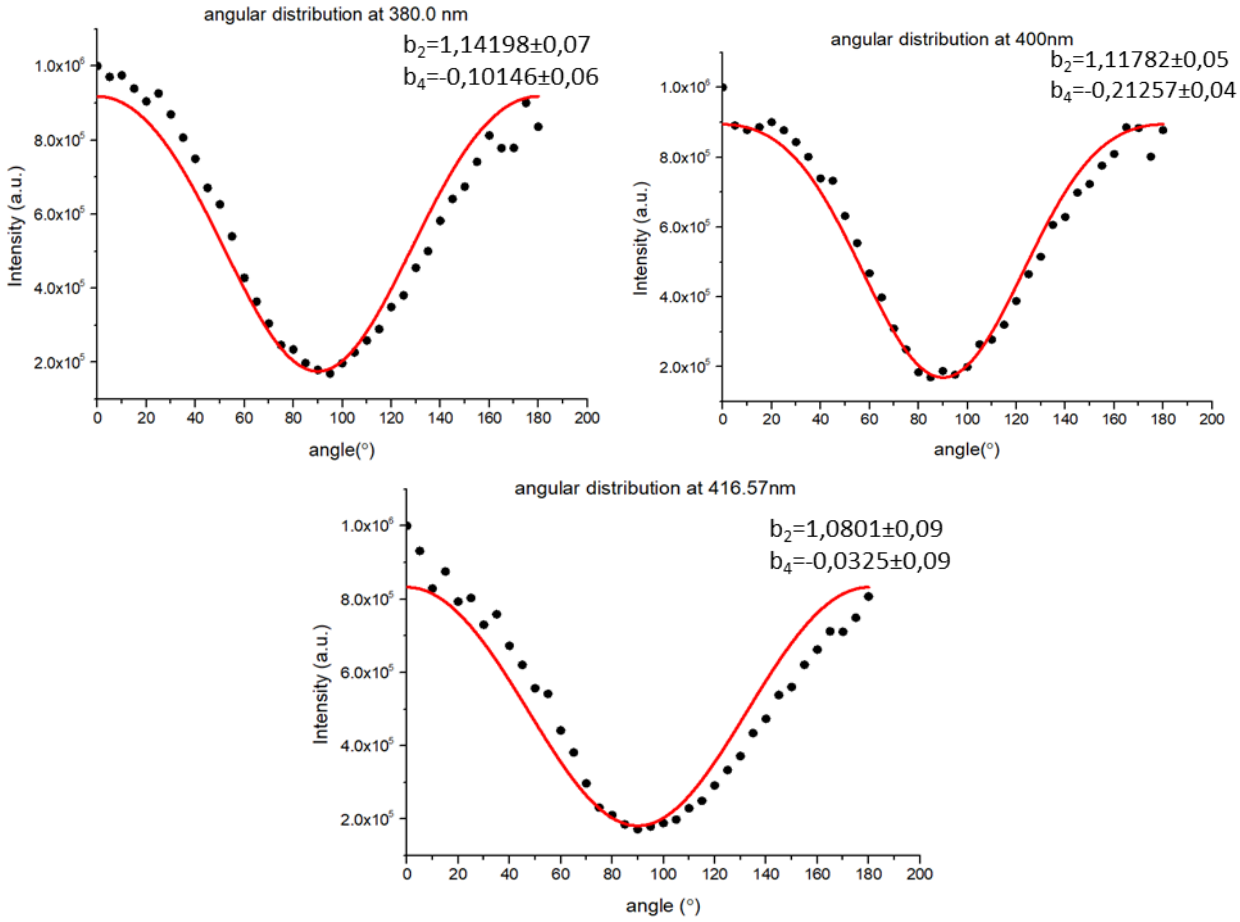


***Figure 5.4: Experimental data for angular distribution of s-(+)-fenchone for different wavelengths and linearly polarized light. The red lines show the fitting in each case.***

The coefficients $b_2$ and $b_4$for s- and r- fenchone are plotted over wavelength in Figure 5.5.

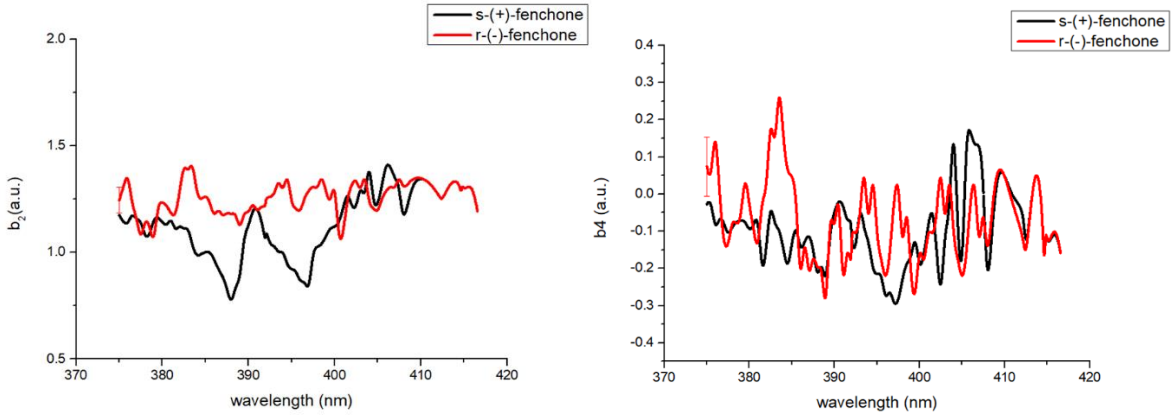


***Figure 5.5: $b_2$ and $b_4$ coefficients plotted over wavelength for the two enantiomers of fenchone.***

From the graph of $b_2$ over wavelength we can see that the two enantiomers don't behave the same way over wavelength. On the contrary, the values of $b_4$ are approximately around zero

and with a big error bar, so we don't take it into account.

Respectively, analyzing the data from the subtraction of the right from left circularly polarized light we obtain the following graphs in Figure 5.6 as well as the values of the coefficients $b_1$, $b_3$ and $b_5$. The intensity distribution is given by:

$$I_p(\theta) = 2b_1^{\{p\}}P_1(cos\theta) + 2b_3^{\{p\}}P_3(cos\theta) + 2b_5^{\{p\}}P_5(cos\theta)$$

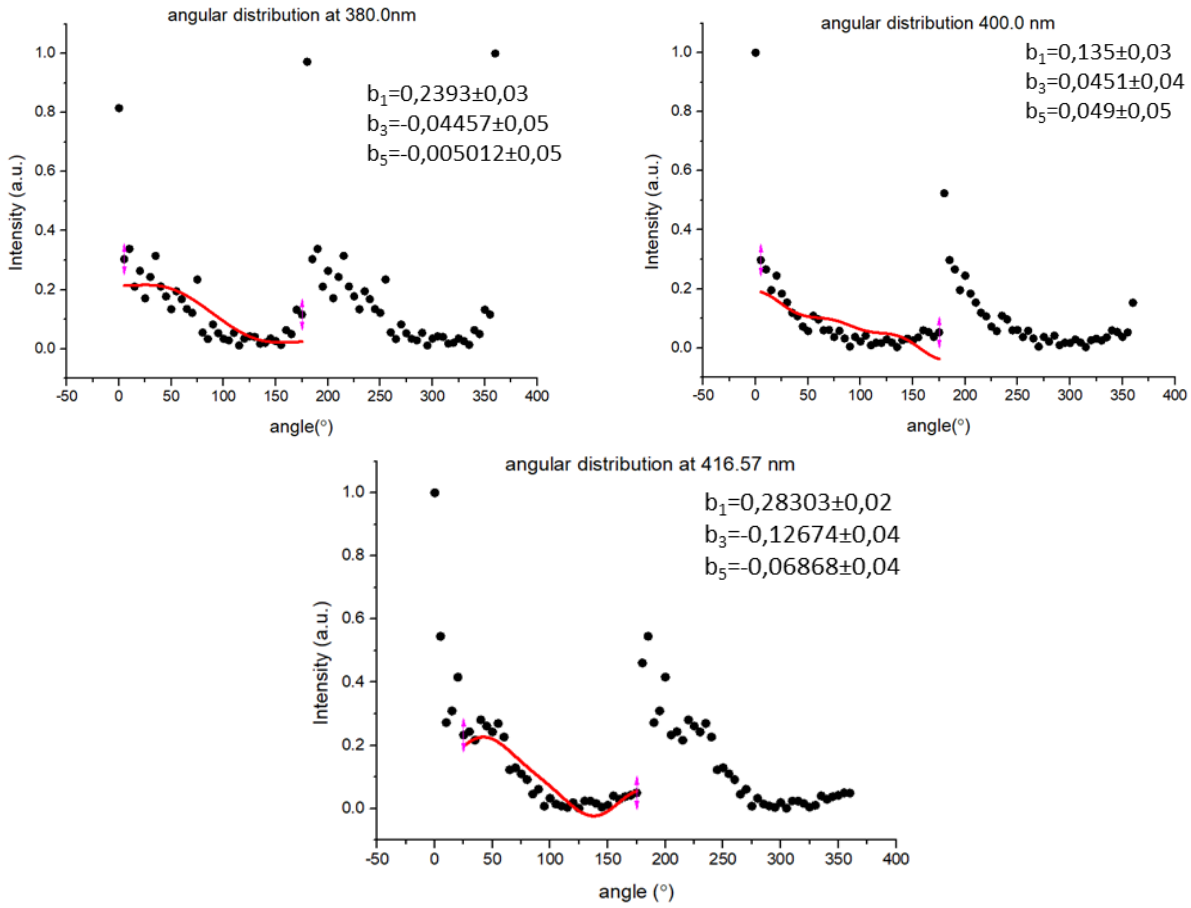


***Figure 5.6: Experimental data for angular distribution of s-(+)-fenchone for different wavelengths and circularly polarized light. The red lines show the fitting in each case.***

The dependence of those three coefficients over wavelength is displayed in Figure 5.7.

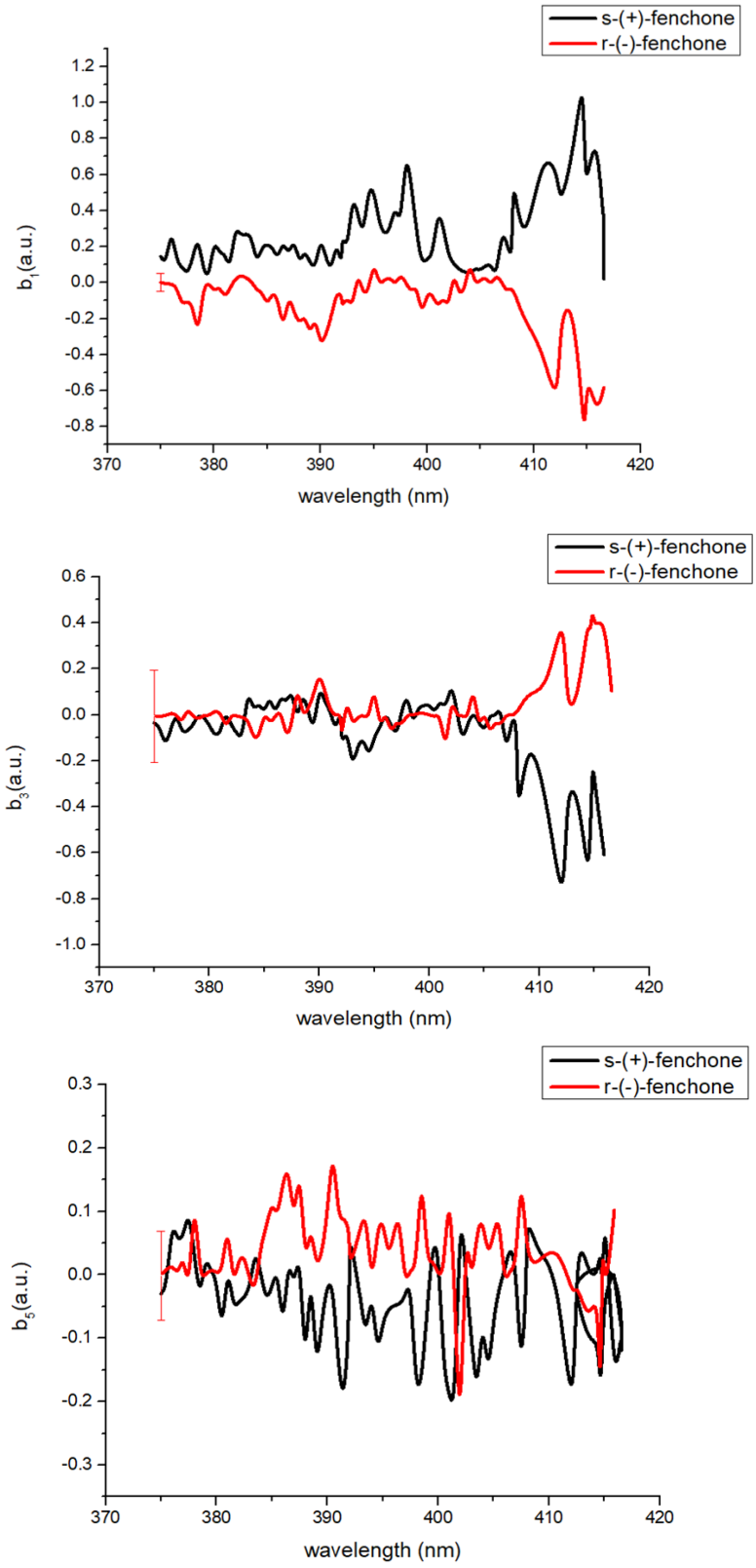


***Figure 5.7: $b_1$, $b_3$ and $b_5$ coefficients plotted over wavelength for the two enantiomers of fenchone.***

It is evident that the values of all the PECD parameters ($b_1$, $b_3$ and$b_5$) change sign from the one enantiomer to the other which proves the PECD effect, the two enantiomers have the same PECD signal but with different sign. In the plots we can see the error bars of each calculation, $b_1$ is more accurate than the others and also has stronger signal, compared to the other two that

is close to zero. Although the signal signature is contained in the odd-order Legendre polynomial coefficient (Chapter 1), the magnitude is usually derived by computing a sum over the odd-order coefficients $b_i$ normalized to the total signal $c_0$ denoted as linear PECD. This value is given by the equation[26]:

$$\mathrm{LPECD} = \frac{1}{c_0}\left(2b_1 - \frac{1}{2}b_3 + \frac{1}{4}b_5\right)$$

The visualization of this signal is depicted in Figure 5.8.

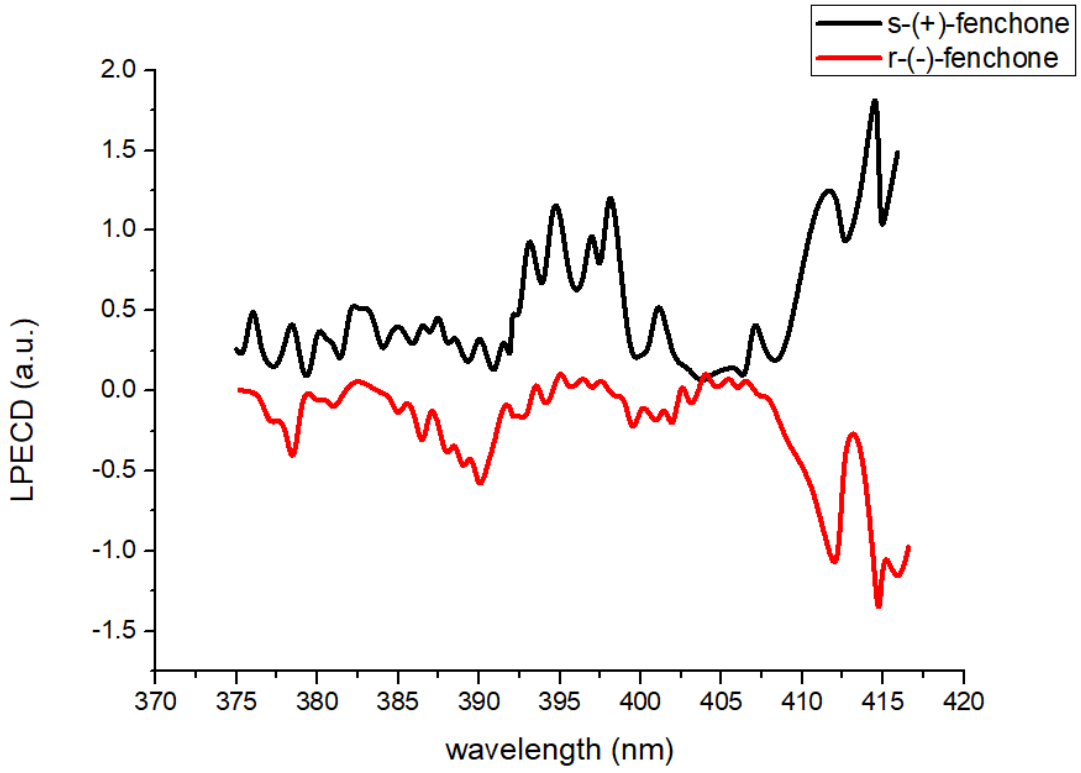


***Figure 5.8: LPECD signal over wavelength for both the enantiomers of fenchone.***

Within the error of our experiment we observe the same magnitude with opposite sign for the two enantiomers without taking into account the enantiomeric purity of 84% for r-(-)-fenchone. This may impact the accuracy of the r-(-)-fenchone's signal. The PECD decreases slightly in magnitude at shorter wavelengths. In addition, this graph is similar to the graph of $b_1$ since it's the one that contributes the most to LPECD.
Another reason for the deviation of the mirror image signal from the two enantiomers may be due to different vibrational states that have been excited from the 3p state since these two electronic states are close to each other.

## 5.3 Summary and future work

In this contribution we demonstrated that PECD can be observed when using an ordinary ns dye laser. We obtained the photoelectron circular dichroism (PECD) of the chiral molecule fenchone after 2+1 REMPI via the 3s Rydberg state for selected ionization energies in the spectral range between 375 nm and 420 nm. We observe the mirror image dependence of the PECD signal of the two enantiomers of fenchone with a few differences though. More experiments need to be

conducted, additional theoretical computations and generally further investigation is necessary in order to be able to explain the deviation observed and fully characterize the way the chiral molecule interferes with circularly polarized light. Also, we're looking forward to study more chiral molecules and see how they respond to PECD, so that we have more information about this effect. Being able to use a commercial ns laser to observe PECD furthermore reduces the technical requirements to apply PECD in analytical chemistry and thus paves the way for many new investigations in chiral recognition in the gas phase.

References

[1] G. A. Garcia, L. Nahon, M. Lebech, J. C. Houver, D. Dowek, I. Powis, J.Chem. Phys. **2003**, 119,781–8784.
[2] T. Lischke, N. Bowering, B. Schmidtke, N. Muller, T. Khalil, U. Heinzmann,Phys. Rev. A **2004**, 70, 022507.
[3] L. Nahon, G. A. Garcia, C. J. Harding, E. A. Mikajlo, I. Powis, J. Chem. Phys.**2006**, 125, 114309.
[4] S. Beaulieu, A. Ferré, R. Géneaux, R. Canonge, D. Descamps, B. Fabre, N. Fedorov, F. Légaré, S. Petit, T. Ruchon, V. Blanchet, Y. Mairesse and B. Pons,New J. Phys. 18, **2016**, 102002.
[5] Anne D. Müller, Anton N. Artemyev, and Philipp V. Demekhin, J. Chem. Phys. 148, **2018**, 214307.
[6] J. Miles, D. Fernandes, A. Young, C.M.M. Bond, S.W. Crane, O. Ghafur, D. Townsend, J. Sa, J.B. Greenwood, Analytica Chimica Acta, 984, **2017**, 134e139.
[7] S. Beaulieu, A. Comby, D. Descamps, B. Fabre, G. A. Garcia, R. Géneaux, A. G. Harvey, F. Légaré , Z. Mašín, L. Nahon, A. F. Ordonez, S. Petit, B. Pons, Y. Mairesse, O. Smirnova and V. Blanchet, Nature Phys Ics, 14, **2018**, 484–489.
[8] C. Lux, A. Senftleben, C. Sarpe, M. Wollenhaupt and T. Baumert, J. Phys. B: At. Mol. Opt. Phys. 49, **2016**, 02LT01 (7pp).
[9] C. Lux, M. Wollenhaupt, C. Sarpe, and T. Baumert, Chem. Phys. Chem., 16, 1, **2015**, 115-137.
[10] L. Nahon, L. Nag,G. Garcia, I. Myrgorodska, U. J. Meierhenrich, S. Beaulieu, V. Wanie, V. lanchet, R. Géneaux and I. Powis,Phys. Chem. Chem. Phys., **2016**,1-25.
[11] I. Powis, C. J. Harding, G. A. Garcia, and L. Nahon, ChemPhysChem, **2008**, 9, 475 – 483.
[12] L. Nahon, G. A. Garcia, I. Powis, Journal of Electron Spectroscopy and Related Phenomena 204, **2015**, 322–334.
[13] A. Ferr´e, A. E. Boguslavskiy, M. Dagan, V. Blanchet, B. D. Bruner, F. Burgy, A. Camper, D. Descamps, B. Fabre, N. Fedorov, J. Gaudin, G. Geoffroy, J. Mikosch, S. Patchkovskii, S. Petit, T. Ruchon, H. Soifer, D. Staedter, I. Wilkinson, A. Stolow, N. Dudovich and Y. Mairesse, Nat. Commun., **2015**, 6, 5952.
[14] A. Ferré, C. Handschin, M. Dumergue, F. Burgy, A. Comby, D. Descamps, B. Fabre, G. A. Garcia, R. Géneaux, L. Merceron, E. Mével, L. Nahon, S. Petit, B. Pons, D. Staedter, S. Weber,T. Ruchon, V. Blanchet and Y. Mairesse, Nature Photonics Letters, Online Publications, **2014**, 1-6.
[15] C. Lux, M. Wollenhaupt, C. Sarpe and T. Baumert, ChemPhysChem, **2015**, 16,115–137.
[16] A. Zhao, P. Sandor, T. Rozgonyi and T. Weinacht, J. Phys. B: At., Mol. Opt. Phys.,**2014**, 47, 204023.
[17] M. Wollenhaupt, New J. Phys. 18, **2016**, 121001.
[18] A. Comby, S. Beaulieu, M. Boggio-Pasqua, D. Descamps, F. Légaré,L. Nahon, S. Petit, B. Pons, B. Fabre, Y. Mairesse, and V. Blanchet,Phys. Chem. Lett., **2016**,722, 4514-4519.
[19] A. Kastner, C. Lux, T. Ring, S. Zìllighoven, C. Sarpe, A. Senftleben, and T. Baumert, ChemPhysChem, **2016**, 17, 1119 – 1122.
[20] A. Kastner, T. Ring, B. C. Krüger, G. B. Park, T. Schäfer, A. Senftleben, and T. Baumert, J. Chem. Phys. 147, **2017**, 013926.
[21] R. Hadidi, D. K. Bozanic, G. A. Garcia & L. Nahon, **2018**, Advances in Physics: X, 3:1, 1477530.
[22] A. F. Ordonez and O. Smirnova, PHYSICAL REVIEW A 98, **2018**, 063428.
[23] A. F. Ordonez and O. Smirnova, PHYSICAL REVIEW A 99, **2019**,043416.
[24] A. Kastner, T. Ring, H. Braun, A. Senftleben, and T. Baumert, ChemPhysChem, 20, **2019**, 1416– 1419.

[25] A. Kastner, C. Lux, T. Ring, S. Züllighoven, C. Sarpe, A. Senftleben and T. Baumert, ChemPhysChem, **2016**, 17, 1119– 1122.
[26] C. Lux, M. Wollenhaupt, C. Sarpe and T. Baumert, ChemPhysChem, **2015**, 16, 115–137.